

Quantum many-body dynamics for fermionic t - J model simulated with atom arrays

Ye-Bing Zhang,^{1,2} Xin-Chi Zhou,^{1,2} Bao-Zong Wang,^{1,2} and Xiong-Jun Liu^{1,2,3,*}

¹*International Center for Quantum Materials and School of Physics, Peking University, Beijing 100871, China*

²*Hefei National Laboratory, Hefei 230088, China*

³*International Quantum Academy, Shenzhen 518048, China*

The fermionic t - J model has been widely recognized as a canonical model for broad range of strongly correlated phases, particularly the high- T_c superconductor. Simulating this model with controllable quantum platforms offers new possibilities to probe high- T_c physics, yet suffering challenges. Here we propose a novel scheme to realize a highly-tunable extended t - J model in a programmable Rydberg-dressed tweezer array. Through engineering the Rydberg-dressed dipole-dipole interaction and inter-tweezer couplings, the fermionic t - J model with independently tunable exchange and hopping couplings is achieved. With the high tunability, we explore quantum many-body dynamics in the large J/t limit, a regime well beyond the conventional optical lattices and cuprates, and predict an unprecedented many-body self-pinning effect enforced by local quantum entanglement with emergent conserved quantities. The self-pinning effect leads to novel nonthermal quantum many-body dynamics, which violates eigenstate thermalization hypothesis in Krylov subspace. Our prediction opens a new horizon in exploring exotic quantum many-body physics with t - J model, and shall also make a step towards simulating the high- T_c physics in neutral atom systems.

Introduction.— The high- T_c superconductivity (SC) in doped cuprates has been discovered for several decades [1], yet a comprehensive understanding of their phase diagram remains elusive [2, 3] due to the limitations of analytical and numerical methods. The quantum simulation based on controllable artificial systems [4–6] has emerged as a promising tool to probe its underlying physics. The Fermi-Hubbard model and related t - J model are recognized as canonical models [7–13] for high- T_c SC. While experimental realizations of the single-band Hubbard model in optical lattices have been widely reported [14–23], these studies face fundamental, non-technical limitations. First, in the Mott regime of single-band Hubbard model, t and $J = 4t^2/U$ are intrinsically linked, constraining the tunability of J/t . In real cuprate materials, however, these parameters can vary more freely, as originated from the three-band model [9, 11, 13]. Second, recent numerical studies suggest that the high- T_c SC crucially depends on the next-nearest-neighbour (NNN) hopping [24–32], which is hard to engineer in optical lattices. Recently a new simulation scheme based on polar molecules [33, 34] have been proposed, while realizing a programmable fermionic t - J model with highly tunable parameters remains an outstanding issue.

Rydberg atoms in tweezer arrays [35–37] may present a promising solution to address the problem. The intrinsic long-range interaction [38–40] render Rydberg atoms powerful quantum simulators for many-body physics [41], especially for quantum spin models [42–50]. Moreover, “Rydberg dressing” [51, 52] enables further control over interaction and lifetime of the system. Applications of Rydberg-dressed atoms have included simulations of supersolid states [53, 54], XYZ spin model [55–57], long-range Ising chain [58] and extended Fermi(Bose)-Hubbard model [59, 60]. However, most of these studies

focus on quantum magnets without charge degree of freedom [44, 45, 55–59]. Recent advancements in coherent transport of tweezers [61–63] and tunnel-coupled tweezers [64–66] realized atom hopping between adjacent tweezers, enabling the realization of Fermi-Hubbard model in tweezer arrays [67, 68] and the fermion tunneling gates [69]. This capability opens up the further simulation of intricate doped quantum magnet in tweezer arrays.

In this letter, we propose a novel scheme to realize the highly tunable fermionic t - J model in a programmable Rydberg-dressed tweezer array, with which we uncover exotic nonthermal quantum many-body dynamics in the large J/t regime, a regime far beyond conventional optical lattices and cuprates, but well achievable in the current realization. The Hamiltonian is given by

$$\begin{aligned} H &= H_{t,N} + H_{t',NN} + H_J, \\ H_{t,N} &= \sum_{\langle i,j \rangle, \sigma} (-t P_i c_{i,\sigma}^\dagger c_{j,\sigma} P_j + \text{H.c.}), \\ H_{t',NN} &= \sum_{\langle\langle i,j \rangle\rangle, \sigma} (-t' P_i c_{i,\sigma}^\dagger c_{j,\sigma} P_j + \text{H.c.}), \\ H_J &= \sum_{i \neq j} [J_{\text{ex},ij} (S_{i,x} S_{j,x} + S_{i,y} S_{j,y}) + \\ &\quad + J_{z,ij} (S_{i,z} S_{j,z} - \frac{1}{4} n_i n_j)], \end{aligned} \quad (1)$$

where $P_i = 1 - n_{i,\uparrow} n_{i,\downarrow}$ excludes double occupancy on site i , with $n_{i,\sigma} = c_{i,\sigma}^\dagger c_{i,\sigma}$ ($\sigma = \uparrow, \downarrow$) the fermion number operator. The kinetic terms $H_{t,N}$ and $H_{t',NN}$ describe hopping processes between nearest-neighbor (NN) sites with amplitude t and NNN sites with amplitude t' , respectively. Our scheme allows a free tuning of spin interaction strength J/t and NNN hopping strength t'/t , a key feature to simulate the high- T_c SC [70]. In the large J/t limit, we show the existence of Hilbert space fragmentation (HSF) [71–74] characterized by the emergent conserved quantities of the local quantum entangled

* Corresponding author: xiongjunliu@pku.edu.cn

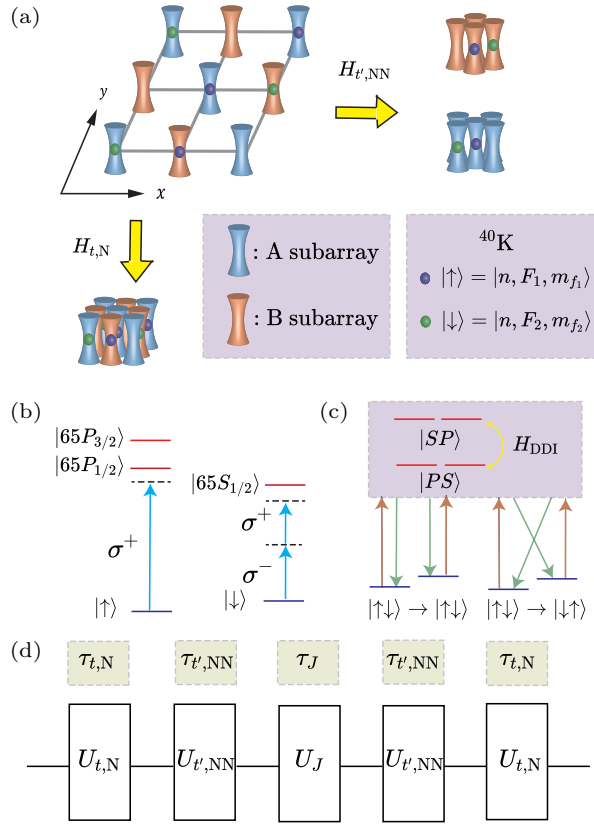


FIG. 1. Scheme for simulating the t - J model. (a) Realization of the NN and NNN hopping terms $H_{t,N}$ and $H_{t',NN}$ in a 2D square tweezer array, which is composed of A and B subarrays. The spin up $|↑\rangle$ and spin down $|↓\rangle$ states are encoded in two hyperfine states of fermionic (e.g. ^{40}K) atoms. (b) Ground states are dressed to the Rydberg states with principle quantum number $n = 65$. $|↑\rangle$ is dressed to states $|65P\rangle$ via a single-photon process using σ^+ polarized light, and $|↓\rangle$ is dressed to state $|65S\rangle$ through a two-photon process involving σ^+ and σ^- polarized light [83]. (c) Realization of the interaction term H_J . The diagonal channels (left) generate the Ising interaction $J_{z,ij}$, while the off-diagonal channels (right) generate the spin exchange interaction $J_{ex,ij}$. (d) A digital combination of the hopping and interaction terms is employed to construct the full t - J Hamiltonian.

states. Most nontrivially, we predict an unprecedented many-body phenomena, dubbed *many-body self-pinning effect*, in which the local quantum entanglement enforces the many-body state to preserve its initial configuration. The self-pinning effect leads to the breakdown of Krylov restricted thermalization, a new mechanism in contrast to previous theory relying on integrability [75–82].

Model realization.—We propose to realize the extended t - J model with a digital combination of inter-tweezer couplings and Rydberg-dressed dipole-dipole interaction (DDI), enabling the realization of both one-dimensional (1D) chain and 2D square array. The fermionic (e.g. ^{40}K) atoms are trapped in optical tweezers, with two ground

$(4^2S_{\frac{1}{2}})$ hyperfine states defining spin states: $|\uparrow\rangle = |F = \frac{9}{2}, m_f = -\frac{9}{2}\rangle$ and $|\downarrow\rangle = |F = \frac{7}{2}, m_f = -\frac{7}{2}\rangle$. The kinetic terms $H_{t,N}$ and $H_{t',NN}$ are realized through controlled atomic tunneling between adjacent tweezers [64–69].

Fig. 1(a) illustrates the realization for the 2D configuration, in which $H_{t,N}$ is realized by coherently coupling the nearest (AB) tweezers, and $H_{t',NN}$ is achieved by coupling only those tweezers within the same AA or BB subarray. The similar subarray-based coupling scheme applies in the 1D case. To eliminate the double occupancy of each tweezer during the tunneling process, one can introduce a strong intra-tweezer repulsion generated by the mature Feshbach resonance technique [84, 86].

The interaction term H_J is realized using dressed DDI, as depicted in Fig. 1(b). The total Hamiltonian is

$$H_J^{\text{tot}} = H_\Omega + H_{\text{DDI}} + H_\Delta, \quad (2)$$

where H_Ω denotes the coupling between ground spin state $|\uparrow\rangle$ (or $|\downarrow\rangle$) and Rydberg p -(or s -)orbital states $|nP\rangle$ (or $|nS\rangle$), with n taken as $n = 65$ below for concrete calculation. H_{DDI} describes dipolar interactions between relevant Rydberg states and H_Δ represents the residual detuning for the coupling between ground and relevant Rydberg states [83]. The spin exchange $J_{ex,ij}$ and Ising interaction $J_{z,ij}$ are derived from the off-diagonal and diagonal contributions of the effective Hamiltonian

$$H_J^{\text{eff}} = \sum_{n=4,6,8,\dots} H_\Omega (GH_\Omega)^{n-1}. \quad (3)$$

Here, $G = (1 - P_0)(E_0 - H_\Delta - H_{\text{DDI}})^{-1}(1 - P_0)$, with P_0 the projection operator in the low-energy subspace spanned by $H_{\text{DDI}} + H_\Delta$, and E_0 is the unperturbed energy. The leading order contribution is illustrated in Fig. 1(c). Specifically, $J_{ex,ij}$ is given by $J_{ex,ij}/2 = \langle \dots \uparrow_i \dots \downarrow_j \dots | H_J^{\text{eff}} | \dots \downarrow_i \dots \uparrow_j \dots \rangle$ and $J_{z,ij}$ is determined by $-(J_{z,ij}/2) = \langle \dots \uparrow_i \dots \downarrow_j \dots | H_J^{\text{eff}} | \dots \uparrow_i \dots \downarrow_j \dots \rangle - \langle \dots \uparrow_i \dots \downarrow_j \dots | H_J^{\text{eff}} (\text{DDI} = 0) | \dots \uparrow_i \dots \downarrow_j \dots \rangle$ [83].

The extended t - J model is realized by the digital combination of $H_{t,N}$, $H_{t',NN}$ and H_J through a sequence illustrated in Fig. 1(d) [88], with the coupling times being $\tau_{t,N}$, $\tau_{t',NN}$, and τ_J , respectively. The time evolution over one cycle is approximated using the standard second-order Suzuki-Trotter decomposition [89–91], yielding the full effective model

$$H_{t-J} = \frac{2\tau_{t,N}}{\tau_J} H_{t_0,N} + \frac{2\tau_{t',NN}}{\tau_J} H_{t'_0,NN} + H_J + o(\tau^2 H^3), \quad (4)$$

where $H_{t_0,N}$ and $H_{t'_0,NN}$ are the bare kinetic terms.

The present scheme directly simulates the extended t - J model, rather than being derived from Hubbard model. This enables a free and independent control of each parameter in H_{t-J} by manipulating $\tau_{t,N}$, $\tau_{t',NN}$, and τ_J . The maximum hopping t and t' can be tuned to be over 0.3 kHz [65], and be further effectively adjusted by the ratio $2\tau_{t,N}(2\tau_{t',NN})/\tau_J$ to be several kHz. The interaction strength $J_{\text{ex}} \approx J_z \approx 2$ kHz is achieved at a distance of

8.2 μm for ^{40}K atoms (see numerical details in Supplementary Material [83]). This allows to realize the broad regimes ranging from $J/t \ll 1$ to $J/t \gg 1$, well surpassing the limitations of simulating Fermi-Hubbard model in optical lattices and beyond the regimes in cuprates.

In experiment the coupling times are restricted by the lifetimes of Rydberg-dressed states (denoted as τ_{dress}) and tweezers (denoted as τ_{tweezer}). In a cryogenic environment at approximately 4 K [92, 93], the lifetime of Rydberg-dressed state is $\tau_{\text{dress}} \approx 60$ ms, which gives $J_{\text{ex},z}\tau_{\text{dress}} \sim 120\hbar$ and is sufficient for the simulation. The lifetime of tweezers τ_{tweezer} can be up to 10^3 seconds [92, 93], far exceeding the total operation time of the present simulation, which is several seconds [83].

HSF with entangled bases.—The high tunability of our scheme enables access to an underexplored parameter regime with $J/t \gg 1$. We focus on the 1D t - J chain with NNN hopping $t' = 0$ and isotropic interaction $J_{\text{ex}} = J_z = J$, with the unimportant anisotropy being neglected [83]. In this regime, the dominant energy scale from H_J induces a novel type of HSF characterized by the quantum entangled states and associated emergent conserved quantities. This contrasts with the previous studies of HSF which is built on product states [71–74, 77–82]. The simplest nontrivial fragmented Krylov subspaces are formed by the three entangled spin bound states as

$$\begin{aligned} |\text{A}\rangle &= \frac{1}{\sqrt{2}}(|\uparrow\downarrow\rangle - |\downarrow\uparrow\rangle), & E_{\text{A}} &= -J, \\ |\text{B}\rangle &= \frac{1}{\sqrt{6}}(|\uparrow\downarrow\downarrow\rangle - 2|\downarrow\uparrow\downarrow\rangle + |\downarrow\downarrow\uparrow\rangle), & E_{\text{B}} &= -\frac{3}{2}J, \\ |\text{C}\rangle &= \frac{1}{\sqrt{6}}(|\downarrow\uparrow\uparrow\rangle - 2|\uparrow\downarrow\uparrow\rangle + |\uparrow\uparrow\downarrow\rangle), & E_{\text{C}} &= -\frac{3}{2}J. \end{aligned} \quad (5)$$

The energies E_i for the state $|i\rangle$ satisfy the relation $3E_{\text{A}} = E_{\text{B}} + E_{\text{C}}$. Then within the Krylov subspace any cluster characterized by three $|\text{A}\rangle$ states can be mixed with that by one $|\text{B}\rangle$ and one $|\text{C}\rangle$ state [94]. Therefore, the three states span dynamically disconnected Krylov subspaces \mathcal{K}_i [see Fig. 2(a)], with each subspace labeled by two emergent conserved quantities $(O_1^{\mathcal{K}_i}, O_2^{\mathcal{K}_i})$:

$$(O_1^{\mathcal{K}_i}, O_2^{\mathcal{K}_i}) = (N_{\text{A}}^{\mathcal{K}_i} + \frac{3}{2}N_{\text{B}}^{\mathcal{K}_i} + \frac{3}{2}N_{\text{C}}^{\mathcal{K}_i}, N_{\text{B}}^{\mathcal{K}_i} - N_{\text{C}}^{\mathcal{K}_i}), \quad (6)$$

where $N_{\text{A}}^{\mathcal{K}_i}$, $N_{\text{B}}^{\mathcal{K}_i}$ and $N_{\text{C}}^{\mathcal{K}_i}$ denote the numbers of the three types of spin bound states. The two quantities remain conserved under allowed transitions between configurations of spin bound states, thereby characterizing the quantum many-body dynamics within the Krylov subspace \mathcal{K}_i . A detailed analysis involving multiple spin states establishes a refined condition, $t/J \ll 0.3714$ and $(t/J)^2 \ll 0.01474$, to fully suppress the transitions between Krylov subspaces and ensure robust HSF [83].

Many-body self-pinning effect.—We predict a highly nontrivial effect, dubbed many-body self-pinning, which emerges in conjunction with robust HSF in the t - J model. This effect, enforced by the entangled nature of spin bound states, hinders transitions between distinct many-body configurations even within the same fragmented subspace. Using the time-evolving block decimation (TEBD) method [95, 96], we first numerically simulate a

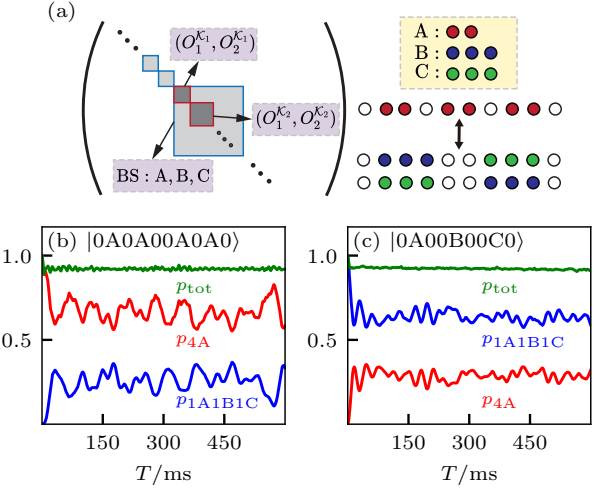


FIG. 2. Hilbert space fragmentation (HSF) and self-pinning effect of 1D t - J model in the $J/t \gg 1$ regime. (a) Matrix representation of the effective Hamiltonian showing dynamically disconnected Krylov subspaces \mathcal{K}_i . Subspaces containing characteristic bound states $|\text{A}\rangle$, $|\text{B}\rangle$ and $|\text{C}\rangle$ are labeled by emergent conserved quantities $(O_1^{\mathcal{K}_i}, O_2^{\mathcal{K}_i})$. Resonant transitions occur between two elementary configurations: one with three $|\text{A}\rangle$ states and another with one $|\text{B}\rangle$ and one $|\text{C}\rangle$ state. (b)-(c) Time evolution of probabilities p_c for observing the configurations $c = \{4\text{A}, 1\text{A}1\text{B}1\text{C}\}$, starting from different initial states in a 14-site chain within the $(O_1^{\mathcal{K}_i}, O_2^{\mathcal{K}_i}) = (4, 1)$ Krylov subspace. $p_{\text{tot}} = p_{4\text{A}} + p_{1\text{A}1\text{B}1\text{C}}$. TEBD simulations use $t=0.1$ kHz, $J=2.0$ kHz, with a bond dimension up to 800.

14-site chain within the $(O_1^{\mathcal{K}_i}, O_2^{\mathcal{K}_i}) = (4, 1)$ Krylov subspace. The basis of this subspace consists of two elementary configurations: one with any valid arrangement of four $|\text{A}\rangle$ states, and another with one $|\text{A}\rangle$, one $|\text{B}\rangle$, and one $|\text{C}\rangle$. The probability p_c of observing these configurations, $c = \{4\text{A}, 1\text{A}1\text{B}1\text{C}\}$, shows that the system evolves within the Krylov subspace labeled by the conserved quantities in Eq. (6) of the initial states. From Fig. 2(b)-(c), the total probability $p_{\text{tot}} = p_{4\text{A}} + p_{1\text{A}1\text{B}1\text{C}} \approx 1$, confirming the HSF of the system. Moreover, the dynamics strongly depend on the initial configuration, retaining a significant population in the initial pattern, manifesting the many-body self-pinning effect.

To elucidate the self-pinning mechanism, we provide a general framework and show how entanglement enforces this effect. Consider a general interacting Hamiltonian $H = \alpha_{\text{kin}}H_{\text{kin}} + \alpha_{\text{int}}H_{\text{int}}$ with kinetic part H_{kin} and interaction part H_{int} in the strong coupling regime $|\alpha_{\text{int}}/\alpha_{\text{kin}}| \gg 1$. For two resonant eigenstates $|\phi_{\text{I}1}\rangle$ and $|\phi_{\text{I}2}\rangle$ of H_{int} , the ratio of the effective energy splitting δ_{eff} to the transition amplitude λ_{eff} induced by H_{kin} is [83]

$$\frac{\delta_{\text{eff}}}{\lambda_{\text{eff}}} = \frac{\sum_{n=n_0^{\delta}}^{\infty} g_n^{\delta}(\alpha_{\text{kin}}^n/\alpha_{\text{int}}^{n-1})}{\sum_{n=n_0^{\lambda}}^{\infty} g_n^{\lambda}(\alpha_{\text{kin}}^n/\alpha_{\text{int}}^{n-1})} \approx \begin{cases} \infty, & n_0^{\lambda} > n_0^{\delta}, \\ \text{const.}, & n_0^{\lambda} = n_0^{\delta}, \\ 0, & n_0^{\lambda} < n_0^{\delta}, \end{cases} \quad (7)$$

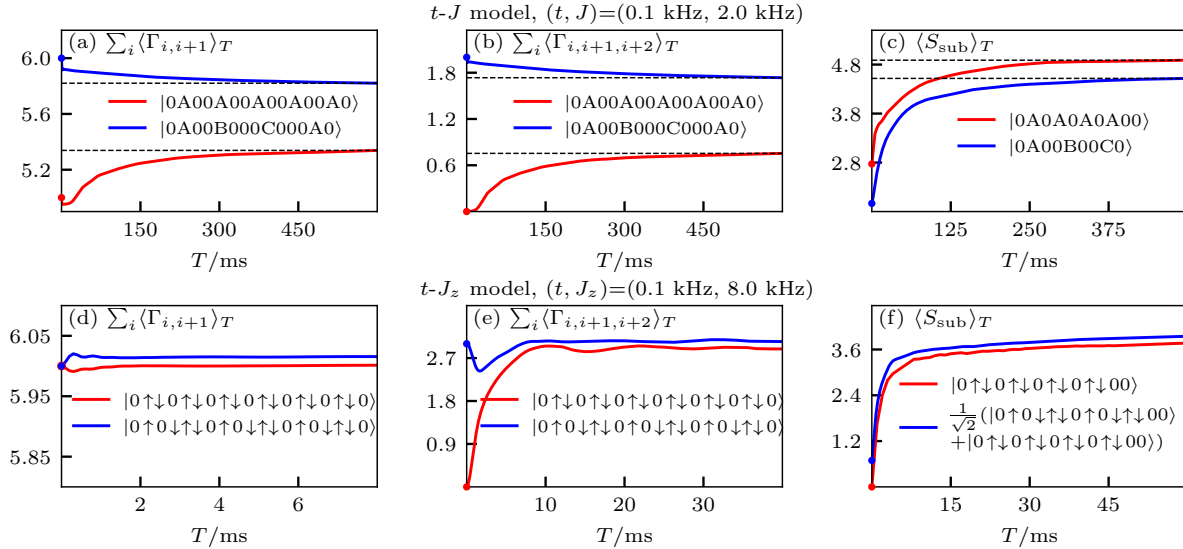


FIG. 3. Nonthermal and thermal dynamics for the t - J model and the t - J_z model. Long-time averages of density correlation operators ($\Gamma_{i,i+1} = n_i n_{i+1}$, $\Gamma_{i,i+1,i+2} = n_i n_{i+1} n_{i+2}$) and sublattice entanglement entropy (EE) are calculated across various initial states for t - J and t - J_z models. (a-c) show the long-time averages of density correlation operators for a 20-site t - J chain and averages of sublattice EE for a 14-site t - J chain, with parameters $t = 0.1$ kHz and $J = 2.0$ kHz. (d-f) show the long-time averages of the density operator for a 19-site t - J_z chain and sublattice EE for a 14-site t - J_z chain, with parameters $t = 0.1$ kHz and $J_z = 8.0$ kHz. Compared to t - J_z model, the long-time averages converge to significantly different values for t - J model. TEBD calculation used the bond dimensions up to 800 for (a-b), 400 for (c), 306 for (d-e), and 100 for (f). The blue and red solid lines in (f) corresponds to two different initial states with the same energy but different S_{sub} .

where n_0^λ and n_0^δ are the leading perturbative orders of λ_{eff} and δ_{eff} , respectively. When $n_0^\delta \leq n_0^\lambda$, transitions between $|\phi_{11}\rangle$ and $|\phi_{12}\rangle$ are suppressed, leaving the quantum state pinned to its initial configuration. Applying this framework to the $(O_1^{\mathcal{K}_1}, O_2^{\mathcal{K}_1}) = (4, 1)$ subspace, detailed calculations for two fundamental configurations reveal $n_0^\lambda = n_0^\delta = 2$ [83], explaining the self-pinning effect.

The self-pinning effect of the 1D t - J model is a consequence of quantum entanglement of the spin bound states spanning the Krylov subspace. The transition between two many-body states with distinct entangled patterns, e.g. the minimal case being that from three A states to one B plus one C states [Fig. 2(a)], necessitates simultaneous tunneling processes of two or more particles, corresponding to second-order or higher-order perturbations. Then the diagonal splitting, as dominated by second-order perturbation, is always relevant and results in the self-pinning effect. In comparison, we examine the t - J_z model [97] with $J_z/t \gg 1$, where the HSF is characterized by product spin bonding states $\uparrow\downarrow \cdots \uparrow\downarrow \cdots$ [98]. The transition can be driven by single-particle tunneling that preserves total number of two-body spin bonds, hence $n_0^\lambda = 1$ while $n_0^\delta \geq 2$, indicating no self-pinning [83].

Nonthermalization in the Krylov subspace.—HSF leads to non-ergodicity and violations of eigenstate thermalization hypothesis (ETH) [99–102] across different subspaces, but thermalization occurs within one non-integrable Krylov subspace [75–80]. The self-pinning effect predicted here renders a new mechanism breaking

ETH within Krylov subspaces of t - J model, which distinguishes it from previous works where non-ergodicity arises from integrability within each subspace [79–82]. We demonstrate the nonthermal (thermal) dynamics for the t - J model (t - J_z model) in the strong coupling limits ($J/t \gg 1$ and $J_z/t \gg 1$). The key distinction lies in the quantum entanglement of few-body states in the t - J model, which drives nonthermalization. Specifically, we analyze the saturated long-time average values of multi-site density correlations $\langle n_i n_{i+1} \rangle_T$ and $\langle n_i n_{i+1} n_{i+2} \rangle_T$, and the sublattice entanglement entropy defined by

$$S_{\text{sub}} = -\text{Tr}[\rho_{\text{sub}} \log(\rho_{\text{sub}})], \quad (8)$$

where $\rho_{\text{sub}} = \text{Tr}_{\text{even sites}}(\rho)$, is the reduced density matrix obtained by tracing out the even sites. The average of an observable O over time T reads $\langle O \rangle_T = (1/T) \int_0^T dt \langle O \rangle$. For t - J model, $\sum_i \langle n_i n_{i+1} \rangle_T$ and $\sum_i \langle n_i n_{i+1} n_{i+2} \rangle_T$ show a strong dependence on the initial states within the same Krylov subspace [Fig. 3(a)-(b)]. These averages converge to distinct values, signaling nonthermalization. For the t - J_z model, the averaged two body-correlation $\sum_i \langle n_i n_{i+1} \rangle_T$ relates to the total number of two-body spin pairs, and thus is constant for any state in the same Krylov subspace, as shown by the coincidence during evolution [Fig. 3(d)]. Further, the average of three-body correlation $\sum_i \langle n_i n_{i+1} n_{i+2} \rangle_T$ saturates to nearly identical values, implying the Krylov-restricted thermalization in t - J_z model [Fig. 3(e)]. The normalized discrepancies approaches zero as the system size increases [83].

The long-time average of the sublattice entanglement entropy $\langle S_{\text{sub}} \rangle_T$ is shown in Fig. 3(c) and (f). For the t - J model, $\langle S_{\text{sub}} \rangle_T$ saturate to distinct values depending on the initial states, whereas for t - J_z model, the values converge. The results demonstrate that within the Krylov subspaces of t - J model, the long-time evolution cannot be described by a single statistical ensemble, while for t - J_z model, Krylov-restricted thermalization occurs. This contrast demonstrates that local entanglement proliferated self-pinning effect is a novel mechanism driving the breakdown of Krylov-restricted thermalization.

Conclusion and outlook.— We have proposed the realization of a highly tunable fermionic extended t - J model through a programmable Rydberg-dressed tweezer array, and predicted an entanglement-enforced self-pinning effect in the $J/t \gg 1$ regime, which renders a new mechanism of violating ETH and Krylov restricted thermalization. The quantum entanglement of the few-body states in the t - J model characterizes a novel type of Hilbert

space fragmentation, and is essential for the predicted non-thermal quantum many-body dynamics. Many interesting issues, such as the dissipative effects which can be engineered in experiment, deserve further investigation. Given the fundamental importance and broad interests of the t - J model, this work opens up an intriguing avenue to explore the exotic quantum many-body physics beyond the conventional optical lattices and cuprates, and provides a controllable quantum platform to investigate the high- T_c SC physics.

Acknowledgments.— This work was supported by National Key Research and Development Program of China (2021YFA1400900), the National Natural Science Foundation of China (Grants No. 12425401 and No. 12261160368), and the Innovation Program for Quantum Science and Technology (Grant No. 2021ZD0302000), and the Shanghai Municipal Science and Technology Major Project (Grant No. 2019SHZDZX01). The TEBD is implemented by Tenpy library [103].

[1] J. G. Bednorz and K. A. Müller, *Possible high T_c superconductivity in the Ba-La-Cu-O system*, *Zeitschrift für Physik B Condensed Matter* **64**, 189 (1986).

[2] B. Keimer, S. A. Kivelson, M. R. Norman, S. Uchida, and J. Zaanen, *From quantum matter to high-temperature superconductivity in copper oxides*, *Nature* **518**, 179 (2015).

[3] X. Zhou, W.-S. Lee, M. Imada, N. Trivedi, P. Phillips, H.-Y. Kee, P. Törmä, and M. Eremets, *High-temperature superconductivity*, *Nature Reviews Physics* **3**, 462 (2021).

[4] J. I. Cirac and P. Zoller, *Goals and opportunities in quantum simulation*, *Nature Physics* **8**, 264 (2012).

[5] I. M. Georgescu, S. Ashhab, and F. Nori, *Quantum simulation*, *Rev. Mod. Phys.* **86**, 153 (2014).

[6] A. J. Daley, I. Bloch, C. Kokail, S. Flannigan, N. Pearson, M. Troyer, and P. Zoller, *Practical quantum advantage in quantum simulation*, *Nature* **607**, 667 (2022).

[7] K. A. Chao, J. Spałek, and A. M. Oleś, *Canonical perturbation expansion of the Hubbard model*, *Phys. Rev. B* **18**, 3453 (1978).

[8] P. W. Anderson, *The Resonating Valence Bond State in La_2CuO_4 and Superconductivity*, *Science* **235**, 1196 (1987).

[9] F. C. Zhang and T. M. Rice, *Effective hamiltonian for the superconducting Cu oxides*, *Phys. Rev. B* **37**, 3759 (1988).

[10] Y. A. Izyumov, *Strongly correlated electrons: the t - J model*, *Physics-Uspekhi* **40**, 445 (1997).

[11] P. A. Lee, N. Nagaosa, and X.-G. Wen, *Doping a Mott insulator: Physics of high-temperature superconductivity*, *Rev. Mod. Phys.* **78**, 17 (2006).

[12] J. Spałek, *t - J model then and now: a personal perspective from the pioneering times*, *Acta Physica Polonica A* **111**, 409 (2007).

[13] M. Ogata and H. Fukuyama, *The t - J model for the oxide high- T_c superconductors*, *Reports on Progress in Physics* **71**, 036501 (2008).

[14] T. Esslinger, *Fermi-Hubbard Physics with Atoms in an Optical Lattice*, *Annual Review of Condensed Matter Physics* **1**, 129 (2010).

[15] Niels Strohmaier, Daniel Greif, Robert Jördens, Leticia Tarruell, Henning Moritz, Tilman Esslinger, Raddeep Sensarma, David Pekker, Ehud Altman, and Eugene Demler, *Observation of Elastic Doublon Decay in the Fermi-Hubbard Model*, *Phys. Rev. Lett.* **104**, 080401 (2010).

[16] R. A. Hart, P. M. Duarte, T.-L. Yang, X. Liu, T. Paiva, E. Khatami, R. T. Scalettar, N. Trivedi, D. A. Huse, and R. G. Hulet, *Observation of antiferromagnetic correlations in the Hubbard model with ultracold atoms*, *Nature* **519**, 211 (2015).

[17] L. W. Cheuk, M. A. Nichols, K. R. Lawrence, M. Okan, H. Zhang, E. Khatami, N. Trivedi, T. Paiva, M. Rigol, and M. W. Zwierlein, *Observation of spatial charge and spin correlations in the 2D Fermi-Hubbard model*, *Science* **353**, 1260 (2016).

[18] A. Mazurenko, C. S. Chiu, G. Ji, M. F. Parsons, M. Kanász-Nagy, R. Schmidt, F. Grusdt, E. Demler, D. Greif, and M. Greiner, *A cold-atom Fermi-Hubbard antiferromagnet*, *Nature* **545**, 462 (2017).

[19] L. Tarruell and L. Sanchez-Palencia, *Quantum simulation of the Hubbard model with ultracold fermions in optical lattices*, *Comptes Rendus Physique* **19**, 365 (2018).

[20] J. Koepsell, J. Vijayan, P. Sompé, F. Grusdt, T. A. Hilker, E. Demler, G. Salomon, I. Bloch, and C. Gross, *Imaging magnetic polarons in the doped Fermi-Hubbard model*, *Nature* **572**, 358 (2019).

[21] A. Bohrdt, L. Homeier, C. Reinmoser, E. Demler, and F. Grusdt, *Exploration of doped quantum magnets with ultracold atoms*, *Annals of Physics* **435**, 168651 (2021).

[22] M. Xu, L. H. Kendrick, A. Kale, Y. Gang, G. Ji, R. T. Scalettar, M. Lebrat, and M. Greiner, *Frustration- and doping-induced magnetism in a Fermi-Hubbard simulator*, *Nature* **620**, 971 (2023).

[23] H.-J. Shao, Y.-X. Wang, D.-Z. Zhu, Y.-S. Zhu, H.-N. Sun, S.-Y. Chen, C. Zhang, Z.-J. Fan, Y. Deng, X.-C. Yao, Y.-A. Chen, and J.-W. Pan, *Antiferromagnetic*

phase transition in a 3D fermionic Hubbard model, *Nature* **632**, 267 (2024).

[24] H.-C. Jiang and T. P. Devereaux, *Superconductivity in the doped Hubbard model and its interplay with next-nearest hopping t'* , *Science* **365**, 1424 (2019).

[25] S. Gong, W. Zhu, and D. N. Sheng, *Robust d-Wave Superconductivity in the Square-Lattice t -J model*, *Phys. Rev. Lett.* **127**, 097003 (2021).

[26] S. Jiang, D. J. Scalapino, and S. R. White, *Ground-state phase diagram of the t - t' - J model*, *Proceedings of the National Academy of Sciences* **118**, e2109978118 (2021).

[27] H.-C. Jiang and S. A. Kivelson, *High Temperature Superconductivity in a Lightly Doped Quantum Spin Liquid*, *Phys. Rev. Lett.* **127**, 097002 (2021).

[28] X. Lu, F. Chen, W. Zhu, D. N. Sheng, and S.-S. Gong, *Emergent Superconductivity and Competing Charge Orders in Hole-Doped Square-Lattice t -J model*, *Phys. Rev. Lett.* **132**, 066002 (2024).

[29] H. Xu, C.-M. Chung, M. Qin, U. Schollwöck, S. R. White, and S. Zhang, *Coexistence of superconductivity with partially filled stripes in the Hubbard model*, *Science* **384**, eadh7691 (2024).

[30] D.-W. Qu, Q. Li, S.-S. Gong, Y. Qi, W. Li, and G. Su, *Phase Diagram, d-wave Superconductivity, and Pseudo-gap of the t - t' - J Model at Finite Temperature*, *Phys. Rev. Lett.* **133**, 256003 (2024).

[31] Y.-F. Jiang, J. Zaanen, T. P. Devereaux, and H.-C. Jiang, *Ground state phase diagram of the doped Hubbard model on the four-leg cylinder*, *Phys. Rev. Res.* **2**, 033073 (2020).

[32] Feng Chen, F. D. M. Haldane, and D. N. Sheng, *Global phase diagram of D-wave superconductivity in the square-lattice t -J model*, *Proc. Natl. Acad. Sci. U.S.A.* **122**, e2420963122 (2025).

[33] C. Miller, A. N. Carroll, J. Lin, H. Hirzler, H. Gao, H. Zhou, M. D. Lukin, and J. Ye, *Two-axis twisting using floquet-engineered xyz spin models with polar molecules*, *Nature* **633**, 332 (2024).

[34] A. N. Carroll, H. Hirzler, C. Miller, D. Wellmitz, S. R. Muleady, J. Lin, K. P. Zamarski, R. R. W. Wang, J. L. Bohn, A. M. Rey, and J. Ye, *Observation of generalized t -J spin dynamics with tunable dipolar interactions*, *Science* **388**, 381–386 (2025).

[35] M. Endres, H. Bernien, A. Keesling, H. Levine, E. R. Anschuetz, A. Krajenbrink, C. Senko, V. Vuletic, M. Greiner, and M. D. Lukin, *Atom-by-atom assembly of defect-free one-dimensional cold atom arrays*, *Science* **354**, 1024 (2016).

[36] D. Barredo, S. de Léséleuc, V. Lienhard, T. Lahaye, and A. Browaeys, *An atom-by-atom assembler of defect-free arbitrary two-dimensional atomic arrays*, *Science* **354**, 1021 (2016).

[37] D. Barredo, V. Lienhard, S. de Léséleuc, T. Lahaye, and A. Browaeys, *Synthetic three-dimensional atomic structures assembled atom by atom*, *Nature* **561**, 79 (2018).

[38] M. Saffman, T. G. Walker, and K. Mølmer, *Quantum information with Rydberg atoms*, *Rev. Mod. Phys.* **82**, 2313 (2010).

[39] C. S. Adams, J. D. Pritchard, and J. P. Shaffer, *Rydberg atom quantum technologies*, *Journal of Physics B: Atomic, Molecular and Optical Physics* **53**, 012002 (2019).

[40] X. Wu, X. Liang, Y. Tian, F. Yang, C. Chen, Y.-C. Liu, M. K. Tey, and L. You, *A concise review of Rydberg atom based quantum computation and quantum simulation*, *Chinese Physics B* **30**, 020305 (2021).

[41] A. Browaeys and T. Lahaye, *Many-body physics with individually controlled Rydberg atoms*, *Nature Physics* **16**, 132 (2020).

[42] S. de Léséleuc, V. Lienhard, P. Scholl, D. Barredo, S. Weber, N. Lang, H. P. Büchler, T. Lahaye, and A. Browaeys, *Observation of a symmetry-protected topological phase of interacting bosons with rydberg atoms*, *Science* **365**, 775 (2019).

[43] T.-H. Yang, B.-Z. Wang, X.-C. Zhou, and X.-J. Liu, *Quantum hall states for Rydberg arrays with laser-assisted dipole-dipole interactions*, *Phys. Rev. A* **106**, L021101 (2022).

[44] C. Chen, G. Bornet, M. Bintz, G. Emperauger, L. Leclerc, V. S. Liu, P. Scholl, D. Barredo, J. Hauschild, S. Chatterjee, M. Schuler, A. M. Läuchli, M. P. Zaletel, T. Lahaye, N. Y. Yao, and A. Browaeys, *Continuous symmetry breaking in a two-dimensional Rydberg array*, *Nature* **616**, 691 (2023).

[45] Y.-H. Chen, B.-Z. Wang, T.-F. J. Poon, X.-C. Zhou, Z.-X. Liu, and X.-J. Liu, *Proposal for realization and detection of Kitaev quantum spin liquid with Rydberg atoms*, *Phys. Rev. Res.* **6**, L042054 (2024).

[46] T. F. J. Poon, X.-C. Zhou, B.-Z. Wang, T.-H. Yang, and X.-J. Liu, *Fractional quantum anomalous hall phase for raman superarray of rydberg atoms*, *Advanced Quantum Technologies* **7**, 2300356 (2024).

[47] H. Labuhn, D. Barredo, S. Ravets, S. de Léséleuc, T. Macrì, T. Lahaye, and A. Browaeys, *Tunable two-dimensional arrays of single Rydberg atoms for realizing quantum Ising models*, *Nature* **534**, 667 (2016).

[48] P. Scholl, M. Schuler, H. J. Williams, A. A. Eberharter, D. Barredo, K.-N. Schymik, V. Lienhard, L.-P. Henry, T. C. Lang, T. Lahaye, A. M. Läuchli, and A. Browaeys, *Quantum simulation of 2D antiferromagnets with hundreds of Rydberg atoms*, *Nature* **595**, 233 (2021).

[49] H. Bernien, S. Schwartz, A. Keesling, H. Levine, A. Omran, H. Pichler, S. Choi, A. S. Zibrov, M. Endres, M. Greiner, V. Vuletić, and M. D. Lukin, *Probing many-body dynamics on a 51-atom quantum simulator*, *Nature* **551**, 579 (2017).

[50] S. Ebadi, T. T. Wang, H. Levine, A. Keesling, G. Semeghini, A. Omran, D. Bluvstein, R. Samajdar, H. Pichler, W. W. Ho, S. Choi, S. Sachdev, M. Greiner, V. Vuletić, and M. D. Lukin, *Quantum phases of matter on a 256-atom programmable quantum simulator*, *Nature* **595**, 227 (2021).

[51] J. E. Johnson and S. L. Rolston, *Interactions between Rydberg-dressed atoms*, *Phys. Rev. A* **82**, 033412 (2010).

[52] J. B. Balewski, A. T. Krupp, A. Gaj, S. Hofferberth, R. Löw, and T. Pfau, *Rydberg dressing: understanding of collective many-body effects and implications for experiments*, *New Journal of Physics* **16**, 063012 (2014).

[53] N. Henkel, R. Nath, and T. Pohl, *Three-Dimensional Roton Excitations and Supersolid Formation in Rydberg-Excited Bose-Einstein Condensates*, *Phys. Rev. Lett.* **104**, 195302 (2010).

[54] N. Henkel, F. Cinti, P. Jain, G. Pupillo, and T. Pohl, *Supersolid Vortex Crystals in Rydberg-Dressed Bose-Einstein Condensates*, *Phys. Rev. Lett.* **108**, 265301 (2012).

[55] R. M. W. van Bijnen and T. Pohl, *Quantum Mag-*

netism and Topological Ordering via Rydberg Dressing near Förster Resonances, *Phys. Rev. Lett.* **114**, 243002 (2015).

[56] A. W. Glaetzle, M. Dalmonte, R. Nath, C. Gross, I. Bloch, and P. Zoller, *Designing Frustrated Quantum Magnets with Laser-Dressed Rydberg Atoms*, *Phys. Rev. Lett.* **114**, 173002 (2015).

[57] L.-M. Steinert, P. Osterholz, R. Eberhard, L. Festa, N. Lorenz, Z. Chen, A. Trautmann, and C. Gross, *Spatially Tunable Spin Interactions in Neutral Atom Arrays*, *Phys. Rev. Lett.* **130**, 243001 (2023).

[58] J. Zeiher, J.-y. Choi, A. Rubio-Abadal, T. Pohl, R. van Bijnen, I. Bloch, and C. Gross, *Coherent Many-Body Spin Dynamics in a Long-Range Interacting Ising Chain*, *Phys. Rev. X* **7**, 041063 (2017).

[59] E. Guardado-Sánchez, B. M. Spar, P. Schauss, R. Belyansky, J. T. Young, P. Bienias, A. V. Gorshkov, T. Iadecola, and W. S. Bakr, *Quench Dynamics of a Fermi Gas with Strong Nonlocal Interactions*, *Phys. Rev. X* **11**, 021036 (2021).

[60] P. Weckesser, K. Srakaew, T. Blatz, D. Wei, D. Adler, S. Agrawal, A. Bohrdt, I. Bloch, and J. Zeiher, *Realization of a Rydberg-dressed extended Bose Hubbard model*, arXiv:2405.20128 (2024).

[61] J. Beugnon, C. Tuchendler, H. Marion, A. Gaëtan, Y. Miroshnychenko, Y. R. P. Sortais, A. M. Lance, M. P. A. Jones, G. Messin, A. Browaeys, and P. Grangier, *Two-dimensional transport and transfer of a single atomic qubit in optical tweezers*, *Nature Physics* **3**, 696 (2007).

[62] D. Bluvstein, H. Levine, G. Semeghini, T. T. Wang, S. Ebadi, M. Kalinowski, A. Keesling, N. Maskara, H. Pichler, M. Greiner, V. Vuletić, and M. D. Lukin, *A quantum processor based on coherent transport of entangled atom arrays*, *Nature* **604**, 451 (2022).

[63] D. Bluvstein, S. J. Evered, A. A. Geim, S. H. Li, H. Zhou, T. Manovitz, S. Ebadi, M. Cain, M. Kalinowski, D. Hangleiter, J. P. Bonilla Ataides, N. Maskara, I. Cong, X. Gao, P. Sales Rodriguez, T. Karolyshyn, G. Semeghini, M. J. Gullans, M. Greiner, V. Vuletić, and M. D. Lukin, *Logical quantum processor based on reconfigurable atom arrays*, *Nature* **626**, 58 (2024).

[64] S. Zhu, Y. Long, W. Gou, M. Pu, and X. Luo, *Tunnel-Coupled Optical Microtraps for Ultracold Atoms*, *Advanced Quantum Technologies* **6**, 2300176 (2023).

[65] A. M. Kaufman, B. J. Lester, C. M. Reynolds, M. L. Wall, M. Foss-Feig, K. R. A. Hazzard, A. M. Rey, and C. A. Regal, *Two-particle quantum interference in tunnel-coupled optical tweezers*, *Science* **345**, 306 (2014).

[66] A. Bergschneider, V. M. Klinkhamer, J. H. Becher, R. Klemt, L. Palm, G. Zürn, S. Jochim, and P. M. Preiss, *Experimental characterization of two-particle entanglement through position and momentum correlations*, *Nature Physics* **15**, 640 (2019).

[67] B. M. Spar, E. Guardado-Sánchez, S. Chi, Z. Z. Yan, and W. S. Bakr, *Realization of a Fermi-Hubbard Optical Tweezer Array*, *Phys. Rev. Lett.* **128**, 223202 (2022).

[68] Z. Z. Yan, B. M. Spar, M. L. Prichard, S. Chi, H.-T. Wei, E. Ibarra-García-Padilla, K. R. A. Hazzard, and W. S. Bakr, *Two-Dimensional Programmable Tweezer Arrays of Fermions*, *Phys. Rev. Lett.* **129**, 123201 (2022).

[69] D. González-Cuadra, D. Bluvstein, M. Kalinowski, R. Kaubruegger, N. Maskara, P. Naldesi, T. V. Zache, A. M. Kaufman, M. D. Lukin, H. Pichler, B. Vermersch, J. Ye, and P. Zoller, *Fermionic quantum processing with programmable neutral atom arrays*, *Proceedings of the National Academy of Sciences* **120**, e2304294120 (2023).

[70] I. P. Moreira, D. Muñoz, F. Illas, C. de Graaf, and M. García-Bach, *A relationship between electronic structure effective parameters and T_c in monolayered cuprate superconductors*, *Chemical Physics Letters* **345**, 183 (2001).

[71] P. Sala, T. Rakovszky, R. Verresen, M. Knap, and F. Pollmann, *Ergodicity Breaking Arising from Hilbert Space Fragmentation in Dipole-Conserving Hamiltonians*, *Phys. Rev. X* **10**, 011047 (2020).

[72] V. Khemani, M. Hermele, and R. Nandkishore, *Localization from Hilbert space shattering: From theory to physical realizations*, *Phys. Rev. B* **101**, 174204 (2020).

[73] T. Kohlert, S. Scherg, P. Sala, F. Pollmann, B. Hebbe Madhusudhana, I. Bloch, and M. Aidelsburger, *Exploring the Regime of Fragmentation in Strongly Tilted Fermi-Hubbard Chains*, *Phys. Rev. Lett.* **130**, 010201 (2023).

[74] D. Adler, D. Wei, M. Will, K. Srakaew, S. Agrawal, P. Weckesser, R. Moessner, F. Pollmann, I. Bloch, and J. Zeiher, *Observation of Hilbert space fragmentation and fractonic excitations in 2D*, *Nature* **636**, 80 (2024).

[75] D. Hahn, P. A. McClarty, and D. J. Luitz, *Information dynamics in a model with Hilbert space fragmentation*, *SciPost Physics* (2021).

[76] S. Moudgalya, B. A. Bernevig, and N. Regnault, *Quantum many-body scars and Hilbert space fragmentation: a review of exact results*, *Reports on Progress in Physics* **85**, 086501 (2022).

[77] L. Zhao, P. R. Datla, W. Tian, M. M. Aliyu, and H. Loh, *Observation of Quantum Thermalization Restricted to Hilbert Space Fragments and \mathbb{Z}_{2k} Scars*, *Phys. Rev. X* **15**, 011035 (2025).

[78] F. Yang, H. Yarloo, H.-C. Zhang, K. Mølmer, and A. E. B. Nielsen, *Probing Hilbert space fragmentation with strongly interacting Rydberg atoms*, *Phys. Rev. B* **111**, 144313 (2025).

[79] S. Moudgalya, A. Prem, R. Nandkishore, N. Regnault, and B. A. Bernevig, *Thermalization and Its Absence within Krylov Subspaces of a Constrained Hamiltonian*, in *Memorial Volume for Shoucheng Zhang*, Chap. 7, pp. 147–209.

[80] Z.-C. Yang, F. Liu, A. V. Gorshkov, and T. Iadecola, *Hilbert-space fragmentation from strict confinement*, *Phys. Rev. Lett.* **124**, 207602 (2020).

[81] G. De Tomasi, D. Hetterich, P. Sala, and F. Pollmann, *Dynamics of strongly interacting systems: From Fock-space fragmentation to many-body localization*, *Phys. Rev. B* **100**, 214313 (2019).

[82] L. Herviou, J. H. Bardarson, and N. Regnault, *Many-body localization in a fragmented Hilbert space*, *Phys. Rev. B* **103**, 134207 (2021).

[83] See more details in Supplementary material., which includes Refs. [14, 51, 62, 63, 65, 92, 93, 98, 103–108].

[84] C. Chin, R. Grimm, P. Julienne, and E. Tiesinga, *Feshbach resonances in ultracold gases*, *Rev. Mod. Phys.* **82**, 1225 (2010).

[85] C. A. Regal, M. Greiner, and D. S. Jin, *Lifetime of Molecule-Atom Mixtures near a Feshbach Resonance in ^{40}K* , *Phys. Rev. Lett.* **92**, 083201 (2004).

[86] The typical bare tunneling coefficient t_0 between ad-

jacent tweezers typically ranges from 100 to 300 Hz [65, 67, 68]. Then an on-site interaction strength over several kHz is sufficient to eliminate the double occupancy, and can be well achieved according to the experiment studies of the Fermi-Hubbard model in optical lattices [15, 16, 18, 23]. Moreover, the lifetime for fermions confined in lattice configurations can be significantly enhanced by suppressing the three-body loss. For ^{40}K atoms in optical lattices in strongly repulsive Mott-insulating regime, the lifetime can be up to 1s [15], much longer than the typical lifetimes in optical dipole traps [85]. The similar long lifetime is expected for the current simulation and is sufficient.

[87] J. A. Hines, S. V. Rajagopal, G. L. Moreau, M. D. Wahrman, N. A. Lewis, O. Marković, and M. Schleier-Smith, *Spin Squeezing by Rydberg Dressing in an Array of Atomic Ensembles*, *Phys. Rev. Lett.* **131**, 063401 (2023).

[88] Unlike more demanding Rydberg dressing in optical lattices, which has also demonstrated experimentally in [59, 60], our present scheme temporally separates the engineering of hoppings and interactions, and confines atoms at longer distance in spatially separated tweezers when dressing is applied. This setting eliminates interatomic distance fluctuations and avoids the complex behavior of DDI at short range, thereby ensuring greater stability and control. The employed control techniques in our scheme are standard and widely used, closely following the established experiments that couple the ground states to Rydberg states to generate many-body correlations [47–50, 57, 62, 63]. Moreover, the stroboscopic dressing sequences method [60, 87], in which the dressing light is applied periodically in short pulses rather than continuously, as applied in our scheme, can further enhance the lifetime of the dressed atoms.

[89] M. Suzuki, *General theory of fractal path integrals with applications to many-body theories and statistical physics*, *Journal of Mathematical Physics* **32**, 400 (1991).

[90] D. W. Berry, G. Ahokas, R. Cleve, and B. C. Sanders, *Efficient Quantum Algorithms for Simulating Sparse Hamiltonians*, *Communications in Mathematical Physics* **270**, 359 (2007).

[91] H. Zhao, M. Bükov, M. Heyl, and R. Moessner, *Making Trotterization Adaptive and Energy-Self-Correcting for NISQ Devices and Beyond*, *PRX Quantum* **4**, 030319 (2023).

[92] K.-N. Schymik, S. Pancaldi, F. Nogrette, D. Barredo, J. Paris, A. Browaeys, and T. Lahaye, *Single Atoms with 6000-Second Trapping Lifetimes in Optical-Tweezer Arrays at Cryogenic Temperatures*, *Phys. Rev. Appl.* **16**, 034013 (2021).

[93] G. Pichard, D. Lim, E. Bloch, J. Vaneeckloo, L. Bourachot, G.-J. Both, G. Mériaux, S. Dutartre, R. Hostein, J. Paris, B. Ximenez, A. Signoles, A. Browaeys, T. Lahaye, and D. Dreon, *Rearrangement of individual atoms in a 2000-site optical-tweezer array at cryogenic temperatures*, *Phys. Rev. Appl.* **22**, 024073 (2024).

[94] Here, these clusters refer to any spatial arrangements of the characteristic spin bound states, with at least one vacuum state separating these states. For instance, $|\text{B}0\text{C}\rangle$, $|\text{C}0\text{B}\rangle$ and $|\text{B}00\text{C}\rangle$ are clusters comprising one B and one C states. Other multiparticle spin bound states, such as four-body and five-body states, lie out of the Krylov subspace considered in the main text. This is because examination of entangled spin states up to seven particles reveals no similar energy degeneracy relation with configurations constructed from $|\text{A}\rangle$, $|\text{B}\rangle$, and $|\text{C}\rangle$. Further, local spin bound states with more particles have negligible impact on the dynamics, as transitions to these states from configurations built by $|\text{A}\rangle$, $|\text{B}\rangle$, and $|\text{C}\rangle$ states occur only via very high-order processes. Nonetheless, they constitute local bases for other fragmented subspaces, and these states serve as the intermediate states in the transition process between $|\text{A}\rangle$, $|\text{B}\rangle$, and $|\text{C}\rangle$ spin bound states [83].

[95] G. Vidal, *Efficient Simulation of One-Dimensional Quantum Many-Body Systems*, *Phys. Rev. Lett.* **93**, 040502 (2004).

[96] U. Schollwöck, *The density-matrix renormalization group in the age of matrix product states*, *Annals of Physics* **326**, 96 (2011).

[97] Here, we consider the 1D tJ_z model whose Hamiltonian is $H_{t-J_z} = \sum_{i,\sigma} (-tP_i c_{i,\sigma}^\dagger c_{i+1,\sigma} P_{i+1} + \text{H.c.}) + \sum_i J_z S_{z,i} S_{z,i+1}$, where $P_i = 1 - n_{i,\uparrow} n_{i,\downarrow}$ is the projection operator excluding double occupancy on site i .

[98] T. Rakovszky, P. Sala, R. Verresen, M. Knap, and F. Pollmann, *Statistical localization: From strong fragmentation to strong edge modes*, *Phys. Rev. B* **101**, 125126 (2020).

[99] J. M. Deutsch, *Quantum statistical mechanics in a closed system*, *Phys. Rev. A* **43**, 2046 (1991).

[100] M. Srednicki, *Chaos and quantum thermalization*, *Phys. Rev. E* **50**, 888 (1994).

[101] M. Rigol, V. Dunjko, and M. Olshanii, *Thermalization and its mechanism for generic isolated quantum systems*, *Nature* **452**, 854 (2008).

[102] J. M. Deutsch, *Eigenstate thermalization hypothesis*, *Reports on Progress in Physics* **81**, 082001 (2018).

[103] J. Hauschild and F. Pollmann, *Efficient numerical simulations with Tensor Networks: Tensor Network Python (TeNPy)*, *SciPost Phys. Lect. Notes* **5** (2018).

[104] N. Šibalić, J. Pritchard, C. Adams, and K. Weatherill, *ARC: An open-source library for calculating properties of alkali Rydberg atoms*, *Computer Physics Communications* **220**, 319 (2017).

[105] L. W. Cheuk, M. A. Nichols, K. R. Lawrence, M. Okan, H. Zhang, and M. W. Zwierlein, *Observation of 2D Fermionic Mott Insulators of ^{40}K with Single-Site Resolution*, *Phys. Rev. Lett.* **116**, 235301 (2016).

[106] D. Greif, M. F. Parsons, A. Mazurenko, C. S. Chiu, S. Blatt, F. Huber, G. Ji, and M. Greiner, *Site-resolved imaging of a fermionic Mott insulator*, *Science* **351**, 953 (2016).

[107] P. Weinberg and M. Bükov, *QuSpin: a Python package for dynamics and exact diagonalisation of quantum many body systems part I: spin chains*, *SciPost Phys.* **2**, 003 (2017).

[108] P. Weinberg and M. Bükov, *QuSpin: a Python package for dynamics and exact diagonalisation of quantum many body systems. Part II: bosons, fermions and higher spins*, *SciPost Phys.* **7**, 020 (2019).

Supplemental Material: Quantum many-body dynamics for fermionic t - J model simulated with atom arrays

S-1. THE RYDBERG-DRESSED STATES

In this section, we detail the dressing of the two ground states with Rydberg states through single-photon and two-photon transitions. To begin, we define the notation for the atomic states employed throughout the context. The ground states are denoted as $|n^{2s+1}L_J, F, m_f\rangle$, where n is the principal quantum number, s is the spin angular momentum quantum number, L refers to the orbital angular momentum quantum number, J is the total electronic angular momentum quantum number, and F and m_f are the total angular momentum quantum number and the associated magnetic quantum number. The Rydberg states are denoted as $|n^{2s+1}L_J, m_j\rangle \otimes |I, m_i\rangle$, where m_j is the magnetic quantum number associated with J , and I and m_i is the nuclear angular momentum quantum number and the associated magnetic quantum number. Due to the weak hyperfine coupling in highly excited Rydberg states, the nuclear spin I remains effectively decoupled from the total electronic angular momentum J .

As illustrated in Fig. S1, the spin-up state $|\uparrow\rangle = |4^2S_{\frac{1}{2}}, F = \frac{9}{2}, m_f = -\frac{9}{2}\rangle$ in the hyperfine manifold of ${}^{40}\text{K}$ is dressed to Rydberg p -orbital states $|P1(2)\rangle = |65^2P_{\frac{1}{2}(\frac{3}{2})}, m_j = \frac{1}{2}\rangle \otimes |I = 4, m_i = -4\rangle$ via a single-photon process using σ^+ polarized light. This process is described by the effective dressing Hamiltonian $H_{\uparrow, \text{dress}} = H_{\Omega, \uparrow} + H_{\Delta, \uparrow}$, where $H_{\Delta, \uparrow}$ represents the on-site detuning and $H_{\Omega, \uparrow}$ describes the coupling between the bare state $|\uparrow\rangle$ and Rydberg p -orbit states, which are given by

$$H_{\Omega, \uparrow} = \sum_i \left(\frac{1}{2} \Omega_{P1} c_{i, P1}^\dagger c_{i, \uparrow} + \frac{1}{2} \Omega_{P2} c_{i, P2}^\dagger c_{i, \uparrow} + \text{H.c.} \right),$$

$$H_{\Delta, \uparrow} = \sum_i (\Delta_{P1} n_{i, P1} + \Delta_{P2} n_{i, P2}). \quad (\text{S1})$$

Here, $\Omega_{P1(2)}$ and $\Delta_{P1(2)}$ denote the transition amplitude and relative detuning between $|P1(2)\rangle$ and $|\uparrow\rangle$. The spin-down state, $|\downarrow\rangle = |4^2S_{\frac{1}{2}}, F = \frac{7}{2}, m_f = -\frac{7}{2}\rangle$, is dressed to Rydberg s -orbital state $|S1\rangle = |65^2S_{\frac{1}{2}}, m_j = \frac{1}{2}\rangle \otimes |I = 4, m_i = -4\rangle$ via a two-photon process involving σ^+ and σ^- polarized light, as shown in Fig. S1. This process incorporates intermediate states $|e1(2)\rangle = |30^2P_{\frac{1}{2}(\frac{3}{2})}, m_j = -\frac{1}{2}\rangle \otimes |I = 4, m_i = -4\rangle$ (highlighted in the purple box in Fig. S1). The effective dressing Hamiltonian including intermediate states for this transition is similarly given by $H_{\downarrow, \text{dress}}^{\text{tot}} = H_{\Omega, \downarrow}^{\text{tot}} + H_{\Delta, \downarrow}^{\text{tot}}$, with $H_{\Delta, \downarrow}^{\text{tot}}$ labeling the on-site detuning and $H_{\Omega, \downarrow}^{\text{tot}}$ represents the coupling between the bare state $|\downarrow\rangle$ and Rydberg s -orbital state,

$$H_{\Omega, \downarrow}^{\text{tot}} = \sum_i \left(\frac{1}{2} \Omega_{\downarrow e1} c_{i, e1}^\dagger c_{i, \downarrow} + \frac{1}{2} \Omega_{\downarrow e2} c_{i, e2}^\dagger c_{i, \downarrow} + \frac{1}{2} \Omega_{e1 S1} c_{i, S1}^\dagger c_{i, e1} + \frac{1}{2} \Omega_{e2 S1} c_{i, S1}^\dagger c_{i, e2} + \text{H.c.} \right),$$

$$H_{\Delta, \downarrow}^{\text{tot}} = \sum_i (\Delta_{e1} n_{i, e1} + \Delta_{e2} n_{i, e2} + \delta_{S1} n_{i, S1}). \quad (\text{S2})$$

Here, $\Omega_{\downarrow e1(2)}$ and $\Omega_{e1(2) S1}$ represent the transition amplitudes between $|\downarrow\rangle$, $|e1(2)\rangle$ and $|S1\rangle$, while $\Delta_{e1(2)}$ and δ_{S1} denote the relative detunings of $|e1(2)\rangle$ and $|S1\rangle$ to $|\downarrow\rangle$. By eliminating the intermediate states $|e1(2)\rangle$, the effective dressing Hamiltonian $H_{\downarrow, \text{dress}}^{\text{tot}}$ is significantly simplified into $H_{\downarrow, \text{dress}} = H_{\Omega, \downarrow} + H_{\Delta, \downarrow}$ as

$$H_{\Omega, \downarrow} = \sum_i \left(\frac{1}{2} \Omega_{S1} c_{i, S1}^\dagger c_{i, \downarrow} + \text{H.c.} \right),$$

$$H_{\Delta, \downarrow} = \sum_i (\Delta_{S1} n_{i, S1}). \quad (\text{S3})$$

Here, Ω_{S1} represents the effective two-photon transition amplitude between $|\downarrow\rangle$ and $|S1\rangle$, while Δ_{S1} denotes the relative detuning between $|S1\rangle$ and $|\downarrow\rangle$ after including corrections from the AC Stark shifts (green box in Fig. S1). Notably, the single-photon (two-photon) process does not couple the spin state $|\downarrow\rangle$ ($|\uparrow\rangle$) to the Rydberg p -orbital (s -orbital) states due to the large single-particle energy difference of approximately 1.286 GHz between $|\uparrow\rangle$ and $|\downarrow\rangle$. This energy difference does not influence H_J^{tot} owing to the particle number conservation of both $|\uparrow\rangle$ and $|\downarrow\rangle$.

The two-photon process introduces an additional coupling channel, connecting $|\downarrow\rangle$ to $|S3\rangle = |65^2S_{\frac{1}{2}}, m_j = -\frac{1}{2}\rangle \otimes |I = 4, m_i = -3\rangle$ through the intermediate state $|e3\rangle = |30^2P_{\frac{3}{2}}, m_j = -\frac{3}{2}\rangle \otimes |I = 4, m_i = -3\rangle$. In the presence of DDI, this channel could in principle induce a resonant transition from $|\uparrow\downarrow\rangle$ to another pair of hyperfine states of ${}^{40}\text{K}$, specifically $|4^2S_{\frac{1}{2}}, F = \frac{9}{2}, m_f = -\frac{7}{2}\rangle$ and $|4^2S_{\frac{1}{2}}, F = \frac{7}{2}, m_f = -\frac{5}{2}\rangle$. However, numerical simulations in Sec. S-5 indicate that, under the experimental parameters described in Sec. S-3, this coupling channel is too weak to produce any physically significant effects and can therefore be safely neglected.

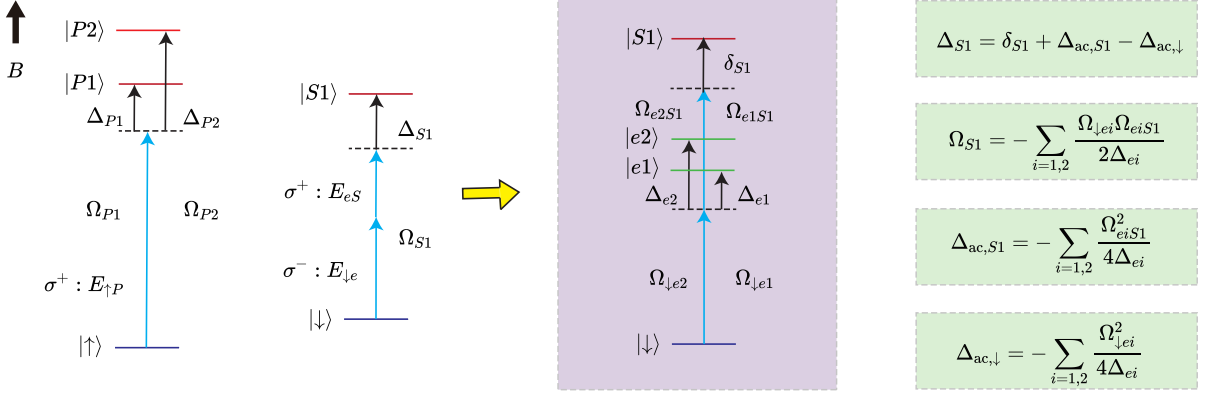


FIG. S1. Detailed sketch of the single-photon and two-photon process. Ω characterizes the transition amplitude between two atom states, and Δ and δ characterize the relative detuning between two atom states. Left: The magnetic field B , perpendicular to the lattice, determine the quantization axis of the ${}^{40}\text{K}$ atoms. $|\uparrow\rangle$ is dressed to Rydberg p -orbital states $|P1(2)\rangle$ via a single-photon process using σ^+ polarized light with the electric field strength $E_{\uparrow P}$. $|\downarrow\rangle$ is dressed to Rydberg s -orbital states $|S1\rangle$ via a two-photon process using σ^+ polarized light with the electric field strength $E_{\downarrow e}$ and σ^- polarized light with the electric field strength E_{eS} . Purple box: detailed sketch of the complete two-photon transition process including the intermediate state $|e1(2)\rangle$. Green box: derivation of parameters of two-photon transitions after the elimination of the intermediate states. $\Delta_{ac,S1}$ and $\Delta_{ac,\downarrow}$ denote the AC Stark shifts for $|S1\rangle$ and $|\downarrow\rangle$.

S-2. DIPOLE-DIPOLE AND VDW INTERACTION

In this section, we detail the relevant Rydberg dipole-dipole and van der Waals (vdW) interaction in our scheme. The Rydberg dipole-dipole interaction (DDI) couples different Rydberg pairs with one p -orbital and one s -orbital. Assuming the quantization axis of atoms determined by the magnetic field is always perpendicular to the lattice, the Rydberg DDI operator is $(\vec{d} = e\vec{r})$

$$V_{\text{DDI}} = \frac{1}{4\pi\epsilon_0} \frac{-0.5d_{1+}d_{2-} - 0.5d_{1-}d_{2+} + d_{1z}d_{2z} - 1.5d_{1+}d_{2+} - 1.5d_{1-}d_{2-}}{x^3}, \quad (\text{S4})$$

where $d_{\pm} = (d_x \pm id_y)/\sqrt{2}$, and x is the distance between two atoms. In our scheme, the operator V_{DDI} ultimately couples a total of 12 Rydberg pairs exhibiting energy differences on the order of DDI, denoted as $|P1S1\rangle, |S1P1\rangle, |P3S2\rangle, |S2P3\rangle, |P2S1\rangle, |S1P2\rangle, |P4S2\rangle, |S2P4\rangle, |P5S2\rangle, |S2P5\rangle, |P6S1\rangle, |S1P6\rangle$. The definition of $|P1(2)\rangle$ and $|S1\rangle$ is given in Sec. S-1, and other states are defined as $|P3\rangle = |65^2P_{\frac{1}{2}}, m_j = -\frac{1}{2}\rangle \otimes |I = 4, m_i = -4\rangle, |P4\rangle = |65^2P_{\frac{3}{2}}, m_j = -\frac{1}{2}\rangle \otimes |I = 4, m_i = -4\rangle, |P5\rangle = |65^2P_{\frac{3}{2}}, m_j = \frac{3}{2}\rangle \otimes |I = 4, m_i = -4\rangle, |P6\rangle = |65^2P_{\frac{3}{2}}, m_j = -\frac{3}{2}\rangle \otimes |I = 4, m_i = -4\rangle, |S2\rangle = |65^2S_{\frac{1}{2}}, m_j = -\frac{1}{2}\rangle \otimes |I = 4, m_i = -4\rangle$. The relevant Hamiltonian H_{DDI} is formulated by the representation of V_{DDI} in the Hilbert space spanned by 12 Rydberg pairs as

$$H_{\text{DDI}} = \sum_{i \neq j, m, n, k, l} \left(\frac{C_{3,(m,n,k,l)}}{|\vec{x}_i - \vec{x}_j|^3} c_{i,Pm}^\dagger c_{j,Sn}^\dagger c_{j,Pk} c_{i,Sl} + \text{H.c.} \right), \quad (\text{S5})$$

where $C_{3,(m,n,k,l)}$ denotes the coefficients of Rydberg DDI and $\vec{x}_{i(j)}$ represents the position vector of atom $i(j)$. Besides, the relative detuning of additional Rydberg p -orbital states to $|\uparrow\rangle$ (denoted as $\Delta_{P3(4,5,6)}$) and additional

s-orbital state to $|\downarrow\rangle$ (denoted as Δ_{S2}) is incorporated as

$$H_{\Delta, \text{DDI}} = \sum_i (\Delta_{P3} n_{i,P3} + \Delta_{P4} n_{i,P4} + \Delta_{P5} n_{i,P5} + \Delta_{P6} n_{i,P6} + \Delta_{S2} n_{i,S2}). \quad (\text{S6})$$

As outlined in the main text, the total Hamiltonian H_J^{tot} can be expressed as $H_{\Omega} + H_{\text{DDI}} + H_{\Delta}$, with $H_{\Omega} = H_{\Omega,\uparrow} + H_{\Omega,\downarrow}$ and $H_{\Delta} = H_{\Delta,\uparrow} + H_{\Delta,\downarrow} + H_{\Delta, \text{DDI}}$.

The Rydberg van der Waals (vdW) interaction H_{vdW} exists between the relevant Rydberg states with the same parity and is formulated as

$$H_{\text{vdW}} = \sum_{i \neq j} \left[\frac{C_{6,P1P1}}{|\vec{x}_i - \vec{x}_j|^6} n_{i,P1} n_{j,P1} + \frac{C_{6,P2P2}}{|\vec{x}_i - \vec{x}_j|^6} n_{i,P2} n_{j,P2} + \frac{C_{6,S1S1}}{|\vec{x}_i - \vec{x}_j|^6} n_{i,S1} n_{j,S1} + \frac{C_{6,P1P2}}{|\vec{x}_i - \vec{x}_j|^6} (n_{i,P1} n_{j,P2} + n_{i,P2} n_{j,P1}) \right], \quad (\text{S7})$$

where C_6 represents the coefficients of Rydberg vdW interaction, and $\vec{x}_{i(j)}$ denotes the position vector of atom $i(j)$. The term H_{vdW} generates the Rydberg-dressed density-density interaction for $|\uparrow\uparrow\rangle$ and $|\downarrow\downarrow\rangle$ [51], expressed as $V_{\uparrow\uparrow,ij} n_{i,\uparrow} n_{j,\uparrow} + V_{\downarrow\downarrow,ij} n_{i,\downarrow} n_{j,\downarrow}$. Numerical simulations in Sec. S-5 show that, under the experimental parameters described in Sec. S-3, $V_{\uparrow\uparrow}$ and $V_{\downarrow\downarrow}$ are negligible compared to J_{ex} and J_z , and are thus omitted from H_J^{tot} .

S-3. EXPERIMENTAL PARAMETERS

In this section, we present the relevant experimental parameters in H_J^{tot} . All the data and calculations are based on the Alkali Rydberg Calculator (ARC) Toolbox [104]. Firstly, we list the typical strengths of the electric fields E of the polarized light and the magnetic field B , as depicted in Fig. S1, in Table S-I.

B	$\mu_B B$	$E_{\uparrow P}$	$E_{\downarrow e}$	E_{eS}
-6.25 G	-8.75 MHz	1.658×10^5 V/m	8.062×10^5 V/m	1.855×10^4 V/m

TABLE S-I. The typical strengths of the electric fields E and the magnetic field B , as depicted in Fig. S1.

Secondly, we list the typical experimental parameters for $H_{\uparrow, \text{dress}}$ [Eq. (S1)] in Table S-II, $H_{\downarrow, \text{dress}}$ [Eq. (S3)] in Table S-III, and $H_{\downarrow, \text{dress}}^{\text{tot}}$ [Eq. S2] in Table S-IV. The lifetime τ is calculated at the cryogenic temperature of 4 K, which is feasible with the current experimental techniques [92, 93].

Ryd.	τ_{Ryd} (4 K)	$\Delta_{P1(2)}/(2\pi)$	$\Omega_{P1(2)}/(2\pi)$	τ_{\uparrow} (4 K)
$65^2 P_{\frac{1}{2}}$	0.956 ms	5.00 MHz	1.29 MHz	58.47 ms
$65^2 P_{\frac{3}{2}}$	0.931 ms	81.08 MHz	1.02 MHz	24.6 s

TABLE S-II. The typical experimental parameters for $H_{\uparrow, \text{dress}}$ in Eq. (S1), as depicted in Fig. S1. τ_{Ryd} denotes the lifetime of $|P1(2)\rangle$, and τ_{\uparrow} denotes the lifetime of $|\uparrow\rangle$ dressed to the Rydberg *p*-orbital states $|P1(2)\rangle$.

Ryd.	τ_{Ryd} (4 K)	$\Delta_{S1}/(2\pi)$	$\Omega_{S1}/(2\pi)$	$\Delta_{ac,S1}/(2\pi)$	$\Delta_{ac,\downarrow}/(2\pi)$	$\delta_{S1}/(2\pi)$	τ_{\downarrow} (4 K)
$65^2 S_{\frac{1}{2}}$	0.287 ms	10.078 MHz	-1.406 MHz	-6.653 MHz	-0.074 MHz	16.657 MHz	58.935 ms

TABLE S-III. The typical experimental parameters for $H_{\downarrow, \text{dress}}$ in Eq. (S3), as depicted in Fig. S1. τ_{Ryd} denotes the lifetime of $|S1\rangle$, and τ_{\downarrow} denotes the lifetime of $|\downarrow\rangle$ dressed to the Rydberg *s*-orbital state $|S1\rangle$.

Ryd.	τ_{Ryd} (4 K)	$\Delta_{e1(2)}/(2\pi)$	$\Omega_{\downarrow e1(2)}/(2\pi)$	τ_{\downarrow} (4 K)	$\Omega_{e1(2)S1}/(2\pi)$
$30^2 P_{\frac{1}{2}}$	0.0886 ms	2000 MHz	20.40 MHz	3.406 s	199.4 MHz
$30^2 P_{\frac{3}{2}}$	0.0862 ms	2887.02 MHz	16.097 MHz	11.09 s	139.5 MHz

TABLE S-IV. The typical experimental parameters for $H_{\downarrow, \text{dress}}^{\text{tot}}$ in Eq. (S2), as depicted in Fig. S1. τ_{Ryd} denotes the lifetime of $|e1(2)\rangle$, and τ_{\downarrow} denotes the lifetime of $|\downarrow\rangle$ dressed to the intermediate states $|e1(2)\rangle$.

Thirdly, we list the C_3 coefficients of the Rydberg DDI for H_{DDI} [Eq. (S5)] in Table S-V (A subtle but important point regarding the use of the ARC toolbox is the definition of d_{\pm} : in ARC, d_{\pm} is defined as $\mp(d_x \pm id_y)/\sqrt{2}$, whereas in our convention it is taken as $(d_x \pm id_y)/\sqrt{2}$). The symmetry of C_3 helps to reduce the number of independent coefficients. For instance, $C_{3,(m,n,k,l)}$ satisfies $C_{3,(m,n,k,l)} = C_{3,(n,m,l,k)}$ by definition, and spin-inversion symmetry further leads to additional constraints. So we only list the non-zero independent C_3 coefficients for H_{DDI} in Table S-V. Besides, we also list the detuning of other relevant Rydberg states for $H_{\Delta,\text{DDI}}$ [Eq. (S6)] in Table S-VI.

$C_{3,(1,1,1,1)}$	$C_{3,(1,1,3,2)}$	$C_{3,(2,1,2,1)}$	$C_{3,(2,1,4,2)}$	$C_{3,(5,2,6,1)}$
2.306 GHz/ μm^3	-6.918 GHz/ μm^3	4.580 GHz/ μm^3	3.435 GHz/ μm^3	10.305 GHz/ μm^3
$C_{3,(1,1,2,1)}$	$C_{3,(1,1,4,2)}$	$C_{3,(1,1,5,2)}$	$C_{3,(2,1,5,2)}$	\sim
-3.250 GHz/ μm^3	4.875 GHz/ μm^3	-2.8145 GHz/ μm^3	-1.983 GHz/ μm^3	\sim

TABLE S-V. The non-zero independent C_3 coefficients for H_{DDI} in Eq. (S5).

$\Delta_{P3}/(2\pi)$	$\Delta_{P4}/(2\pi)$	$\Delta_{P5}/(2\pi)$	$\Delta_{P6}/(2\pi)$	$\Delta_{S2}/(2\pi)$
10.83 MHz	92.75 MHz	69.42 MHz	104.41 MHz	34.16 MHz

TABLE S-VI. The detuning of other relevant Rydberg states for $H_{\Delta,\text{DDI}}$ in Eq. (S6).

Finally, we list the C_6 coefficients of the Rydberg vdW interaction for H_{vdW} [Eq. (S7)] in Table S-VII.

$C_{6,P1P1}$	$C_{6,P2P2}$	$C_{6,P1P2}$	$C_{6,S1S1}$
228.5 GHz/ μm^3	188.94 GHz/ μm^3	-148.53 GHz/ μm^3	-36.46 GHz/ μm^3

TABLE S-VII. The C_6 coefficients for H_{vdW} in Eq. (S7).

S-4. PERTURBATION ESTIMATIONS OF J_{ex} AND J_z

In this section, we give an estimation of J_{ex} and J_z by perturbation theory. The total Hamiltonian H_J^{tot} is decomposed into two parts: $H_{\text{DDI}} + H_{\Delta}$ serves as the unperturbed Hamiltonian, while H_{Ω} is treated as the perturbation. Only even-order perturbation processes contribute to the low-energy effective Hamiltonian H_J^{eff} within the low-energy subspace composed of spin states $|\uparrow\rangle$ and $|\downarrow\rangle$. Noting that the second-order perturbation processes constitute pure single-particle energy corrections, their contribution adds up to a constant due to the conservation of particle number for both $|\uparrow\rangle$ and $|\downarrow\rangle$. Therefore, the low-energy effective Hamiltonian is formulated as

$$H_J^{\text{eff}} = \sum_{n=4,6,8,\dots} H_{\Omega}(GH_{\Omega})^{n-1}, \quad (\text{S8})$$

where $G = (1 - P_0)(E_0 - H_{\Delta} - H_{\text{DDI}})^{-1}(1 - P_0)$. Here P_0 is the projection operator in the low-energy subspace, and E_0 is the unperturbed energy. We begin by considering only the leading-order term in the effective Hamiltonian, namely the fourth-order process of the form $H_{\Omega}GH_{\Omega}GH_{\Omega}GH_{\Omega}$ in H_J^{eff} .

To obtain the unperturbed eigenstates, we need to diagonalize $H_{\Delta} + H_{\text{DDI}}$. However, if all the relevant twelve Rydberg pairs are considered, the full matrix can not be diagonalized analytically. As a first estimation of J_{ex} and J_z , we reserve only four main bases with the ordering as $|P1S1\rangle$, $|S1P1\rangle$, $|P3S2\rangle$, $|S2P3\rangle$. The matrix representation of $H_{\Delta} + H_{\text{DDI}}$ with these four main bases is

$$H_{\Delta} + H_{\text{DDI}} = \begin{pmatrix} \Delta_{P1} + \Delta_{S1} & W_1(x) & 0 & W_2(x) \\ W_1(x) & \Delta_{P1} + \Delta_{S1} & W_2(x) & 0 \\ 0 & W_2(x) & \Delta_{P3} + \Delta_{S2} & W_1(x) \\ W_2(x) & 0 & W_1(x) & \Delta_{P3} + \Delta_{S2} \end{pmatrix} = \Delta_{+}I \otimes I + \Delta_{-}\sigma_z \otimes I + W_1(x)I \otimes \sigma_x + W_2(x)\sigma_x \otimes \sigma_x. \quad (\text{S9})$$

Here $\Delta_{\pm} = [(\Delta_{P1} + \Delta_{S1}) \pm (\Delta_{P3} + \Delta_{S2})]/2$, $W_1(x) = C_{3,(1,1,1,1)}/x^3$, $W_2(x) = C_{3,(1,1,3,2)}/x^3$, and x is the two-atom

distance. The four eigenstates and corresponding energies of matrix (S9) are

$$\begin{aligned} |\psi_{+,1}\rangle &= \cos\left(\frac{\theta}{2}\right)|P1S1_+\rangle + \sin\left(\frac{\theta}{2}\right)|P3S2_+\rangle, & E_{+,1} &= \Delta_+ + W_1 + \sqrt{\Delta_-^2 + W_2^2}, \\ |\psi_{+,2}\rangle &= -\sin\left(\frac{\theta}{2}\right)|P1S1_+\rangle + \cos\left(\frac{\theta}{2}\right)|P3S2_+\rangle, & E_{+,2} &= \Delta_+ + W_1 - \sqrt{\Delta_-^2 + W_2^2}, \\ |\psi_{-,1}\rangle &= \cos\left(\frac{\theta}{2}\right)|P1S1_-\rangle + \sin\left(\frac{\theta}{2}\right)|P3S2_-\rangle, & E_{-,1} &= \Delta_+ - W_1 + \sqrt{\Delta_-^2 + W_2^2}, \\ |\psi_{-,2}\rangle &= -\sin\left(\frac{\theta}{2}\right)|P1S1_-\rangle + \cos\left(\frac{\theta}{2}\right)|P3S2_-\rangle, & E_{-,2} &= \Delta_+ - W_1 - \sqrt{\Delta_-^2 + W_2^2}. \end{aligned} \quad (\text{S10})$$

Here $\tan(\theta) = W_2/\Delta_-$, and $|P1S1_{\pm}\rangle = (|P1S1\rangle \pm |S1P1\rangle)/\sqrt{2}$, $|P3S2_{\pm}\rangle = (\pm|P3S2\rangle + |S2P3\rangle)/\sqrt{2}$.

Then J_{ex} and J_z can be estimated. Since $J_{\text{ex},ij}(S_{i,x}S_{j,x} + S_{i,y}S_{j,y})$ leads to the exchange process between $|\uparrow\downarrow\rangle$ and $|\downarrow\uparrow\rangle$, the specific value of J_{ex} can be determined as

$$J_{\text{ex}} = 2\langle\downarrow\uparrow|H_J^{\text{eff}}|\uparrow\downarrow\rangle. \quad (\text{S11})$$

And the fourth-order off-diagonal channels of H_J^{eff} generating J_{ex} are

$$|\uparrow\downarrow\rangle \xrightarrow{H_{\Omega}} |\uparrow S1\rangle, |P1(2)\downarrow\rangle \xrightarrow{H_{\Omega}} |\psi_{+,1(2)}\rangle, |\psi_{-,1(2)}\rangle \xrightarrow{H_{\Omega}} |S1\uparrow\rangle, |\downarrow P1(2)\rangle \xrightarrow{H_{\Omega}} |\downarrow\uparrow\rangle. \quad (\text{S12})$$

The detailed calculations provide an analytical estimation of J_{ex} as

$$J_{\text{ex}} = 2\left(\frac{\Omega_{P1}}{2\Delta_{P1}}\right)^2\left(\frac{\Omega_{S1}}{2\Delta_{S1}}\right)^2 \frac{(\Delta_{P1} + \Delta_{S1})^2(\Delta_+^2 W_1 - W_1^3 + W_1 \Delta_-^2 + W_1 W_2^2 - 2\Delta_- \Delta_+ W_1)}{[(\Delta_+ - W_1)^2 - (\Delta_-^2 + W_2^2)][(\Delta_+ + W_1)^2 - (\Delta_-^2 + W_2^2)]}. \quad (\text{S13})$$

The Ising interaction $J_{z,ij}(S_{i,z}S_{j,z} - 1/4n_i n_j)$ can be reformulate as the density-density interaction $-J_{z,ij}/2(n_{i,\uparrow}n_{j,\downarrow} + n_{i,\downarrow}n_{j,\uparrow})$ with no double occupancy. However, the matrix element $\langle\uparrow\downarrow|H_J^{\text{eff}}|\uparrow\downarrow\rangle$ contains the contribution of single-particle energy corrections which add up to a constant. The specific value of J_z should be determined as

$$J_z = -2(\langle\uparrow\downarrow|H_J^{\text{eff}}|\uparrow\downarrow\rangle - \langle\uparrow\downarrow|H_J^{\text{eff}}(W=0)|\uparrow\downarrow\rangle). \quad (\text{S14})$$

Here $H_J^{\text{eff}}(W=0)$ represents the low-energy effective Hamiltonian when $H_{\text{DDI}} = 0$, which contains all the contribution of single-particle corrections. And the fourth-order diagonal channels of H_J^{eff} generating J_z are

$$\begin{aligned} |\uparrow\downarrow\rangle &\xrightarrow{H_{\Omega}} |\uparrow S1\rangle, |P1(2)\downarrow\rangle \xrightarrow{H_{\Omega}} |\psi_{+,1(2)}\rangle, |\psi_{-,1(2)}\rangle \xrightarrow{H_{\Omega}} |\uparrow S1\rangle, |P1(2)\downarrow\rangle \xrightarrow{H_{\Omega}} |\uparrow\downarrow\rangle, \\ |\downarrow\uparrow\rangle &\xrightarrow{H_{\Omega}} |\downarrow P1(2)\rangle, |S1\uparrow\rangle \xrightarrow{H_{\Omega}} |\psi_{+,1(2)}\rangle, |\psi_{-,1(2)}\rangle \xrightarrow{H_{\Omega}} |S1\uparrow\rangle, |\downarrow P1(2)\rangle \xrightarrow{H_{\Omega}} |\downarrow\uparrow\rangle. \end{aligned} \quad (\text{S15})$$

Detailed calculations also provide an analytical estimation of J_z as

$$J_z = -\left(\frac{\Omega_{P1}}{2\Delta_{P1}}\right)^2\left(\frac{\Omega_{S1}}{2\Delta_{S1}}\right)^2(\Delta_{P1} + \Delta_{S1})^2 \left[\frac{\Delta_- - \Delta_+ + W_1}{(\Delta_+ + W_1)^2 - (\Delta_-^2 + W_2^2)} + \frac{\Delta_- - \Delta_+ - W_1}{(\Delta_+ - W_1)^2 - (\Delta_-^2 + W_2^2)} + \frac{2}{\Delta_+ + \Delta_-} \right]. \quad (\text{S16})$$

The estimations derived in Eq. (S13) and (S16) are compared with the numerical simulations shown in Sec. S-5 (See Fig. S2), using the experimental parameters in Sec. S-3. As illustrated in Fig. S2, the perturbation analysis actually provide a preliminary estimation for J_{ex} and J_z at the two-atom distance $x \approx 8.2 \mu\text{m}$, corresponding to the selected lattice spacing. The discrepancies between analytical estimations and numerical simulations arise from the contribution of higher-order perturbations and those omitted Rydberg pairs.

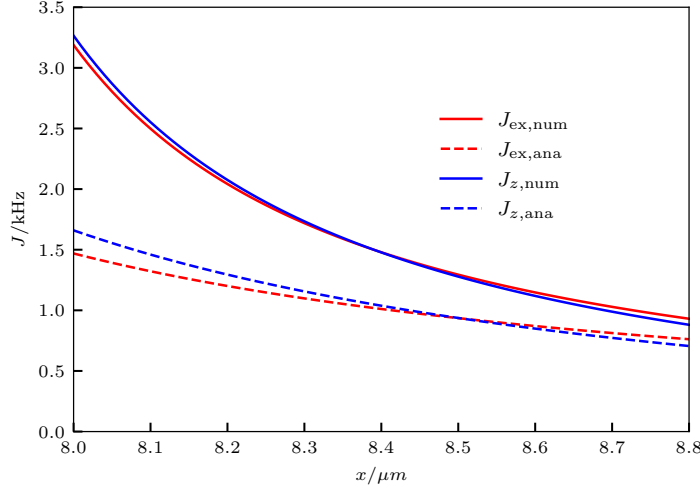


FIG. S2. Comparison between the numerical simulations and the analytical estimations for J_{ex} and J_z . The solid lines represent the J_{ex} and J_z determined by numerical method explained in Sec. S-5, while the dashed lines represent the J_{ex} and J_z determined by analytical estimation in this section.

The physical origin of J_{ex} and J_z can be understood in terms of the dynamical evolution of Rydberg pair states. Since the interaction strength is comparable to the detuning under the chosen parameters, the DDI cannot be treated perturbatively. Instead, the DDI induces coherent oscillations between the Rydberg pair states $|PS\rangle$ and $|SP\rangle$. Starting from the ground state $|\uparrow\downarrow\rangle$, the coupling light drives second-order transitions to $|PS\rangle$. Then DDI subsequently generates a coherent oscillation between $|PS\rangle$ and $|SP\rangle$, which are then coupled back to the ground-state manifold via second-order processes: the return to $|\uparrow\downarrow\rangle$ yields J_z , while the transition to $|\downarrow\uparrow\rangle$ yields J_{ex} . The near-equality of J_{ex} and J_z observed in Fig. S2 reflects underlying coherent oscillation dynamics so wherein two types of transitions channels play equally essential roles.

S-5. NUMERICAL SIMULATIONS OF J_{ex} , J_z , $V_{\uparrow\uparrow}$ AND $V_{\downarrow\downarrow}$

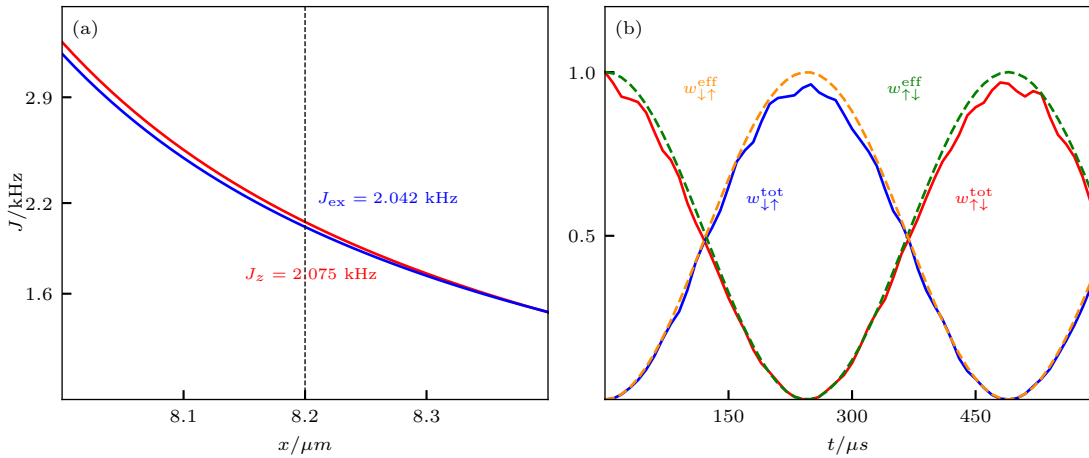


FIG. S3. Estimation of J_{ex} , J_z , and validation of the effective Hamiltonian H_J^{eff} . (a) The effective interaction strengths J_{ex} and J_z are plotted as functions of the two-atom distance x . An appropriate distance of $8.2 \mu\text{m}$ is selected, yielding $J_{\text{ex}} \approx J_z \approx 2 \text{ kHz}$. (b) The time evolution of the system is compared using the total Hamiltonian H_J^{tot} (solid line) and the effective Hamiltonian H_J^{eff} (dashed line). The initial state is chosen as the two-particle state $|\uparrow\downarrow\rangle$. The evolved wave function is expressed as $|\psi(t)\rangle = c_{\uparrow\downarrow}(t)|\uparrow\downarrow\rangle + c_{\downarrow\uparrow}(t)|\downarrow\uparrow\rangle + |\text{others}\rangle$, then the probabilities $w_{\uparrow\downarrow} = |c_{\uparrow\downarrow}|^2$ and $w_{\downarrow\uparrow} = |c_{\downarrow\uparrow}|^2$ are shown as functions of time.

In this section, we explain the details of numerical simulation for J_{ex} , J_z , and the strength of density-density interaction $V_{\uparrow\uparrow}$, $V_{\downarrow\downarrow}$ induced by the Rydberg vdW interaction. For J_{ex} and J_z , the total Hamiltonian H_J^{tot} is diagonalized in a two-site system within the subspace composed of $|\uparrow\downarrow\rangle$, $|\downarrow\uparrow\rangle$ and all the relevant two-site states. Two special eigenstates are identified as $|s_{\pm}\rangle \approx (|\uparrow\downarrow\rangle \pm |\downarrow\uparrow\rangle)/\sqrt{2}$ with the eigenvalues γ_{\pm} . And the matrix representation of the effective Hamiltonian H_J^{eff} , describing the quantum dynamics within subspace composed of $|\uparrow\downarrow\rangle$ and $|\downarrow\uparrow\rangle$, is

$$H_J^{\text{eff}} = \begin{pmatrix} -\frac{J_z}{2} + \delta_{\text{single}} & \frac{J_{\text{ex}}}{2} \\ \frac{J_{\text{ex}}}{2} & -\frac{J_z}{2} + \delta_{\text{single}} \end{pmatrix}. \quad (\text{S17})$$

Here δ_{single} is the single-particle energy shift with $H_{\text{DDI}} = 0$ for $|\uparrow\downarrow\rangle$ and $|\downarrow\uparrow\rangle$. Through matching the eigenvalues of H_J^{eff} and H_J^{tot} , J_{ex} and J_z are determined as

$$\begin{aligned} J_{\text{ex}} &= \gamma_+ - \gamma_-, \\ J_z &= -\gamma_+ - \gamma_- + 2\delta_{\text{single}}. \end{aligned} \quad (\text{S18})$$

Fig. S3(a) shows the numerically determined J_{ex} and J_z as functions of two-atom distance x , using the experimental parameters in Sec. S-3. To choose a suitable lattice spacing, an important consideration is that the energies of the relevant Rydberg pairs may be resonant with the energy of $|\uparrow\downarrow\rangle$ at some special two-atom distances, resulting in the breakdown of perturbation theory and the divergence of J_{ex} and J_z . To avoid the undesirable resonance and generate reasonable J_{ex} and J_z , the lattice spacing a is selected as $8.2 \mu\text{m}$. And the numerically determined J_{ex} and J_z under different two-atom distances are displayed in Table S-VIII. As mentioned in Sec. S-1, the two-photon coupling between $|\downarrow\rangle$ and $|S3\rangle$ may lead to undesirable outcomes. The numerical simulations including atom states relevant to $|S3\rangle$ reveal that, using the experimental parameters in Sec. S-3, the impact of the new coupling channel is just a tiny correction of J_{ex} and J_z , as shown in Table S-IX. The validity of the effective Hamiltonian is further confirmed by comparing the time evolution of a two-site system using the total Hamiltonian H_J^{tot} (atom states relevant to $|S3\rangle$ are included here) and the effective Hamiltonian H_J^{eff} in Eq. (S17), as illustrated in Fig. S3(b).

x	a (8.2 μm)	$\sqrt{2}a$	$2a$	$3a$
J_{ex}	2.0548 kHz	0.2199 kHz	0.0698 kHz	0.0204 kHz
J_z	2.0879 kHz	0.1125 kHz	0.0132 kHz	0.00115 kHz

TABLE S-VIII. J_{ex} and J_z as functions of two-atom distance x , obtained by diagonalization of H_J^{tot} in a two-site system.

x	a (8.2 μm)	$\sqrt{2}a$	$2a$	$3a$
J_{ex}	2.0421 kHz	0.2188 kHz	0.0695 kHz	0.0203 kHz
J_z	2.0752 kHz	0.1119 kHz	0.0131 kHz	0.00114 kHz

TABLE S-IX. J_{ex} and J_z as functions of two-atom distance x with states relevant to $|S3\rangle$.

For the numerical simulations of $V_{\uparrow\uparrow}$ and $V_{\downarrow\downarrow}$, the established method involves comparing the energies of $|\uparrow\uparrow\rangle$ and $|\downarrow\downarrow\rangle$ with and without the Rydberg Vdw interactions [51]. The summarized outcomes are presented in Table S-X, using the model parameters in Sec. S-3. And these results indicate that $V_{\uparrow\uparrow}, V_{\downarrow\downarrow} \ll J_{\text{ex}}, J_z$ in general.

x	a (8.2 μm)	$\sqrt{2}a$	$2a$
$V_{\uparrow\uparrow}$	0.174 kHz	0.0232 kHz	2.93×10^{-3} kHz
$V_{\downarrow\downarrow}$	-2.78×10^{-3} kHz	-3.46×10^{-4} kHz	-4.32×10^{-5} kHz

TABLE S-X. $V_{\uparrow\uparrow}$ and $V_{\downarrow\downarrow}$ as functions of two-atom distance x .

S-6. LIFETIME ESTIMATION

A. Preservation of coherent oscillation: our scheme v.s. optical lattice

Firstly, we analyze the coupling time restricted by the lifetime of Rydberg-dressed state (denoted as τ_{dress}), through comparison with the Fermi-Hubbard model in optical lattices in the harmonic trap. $J\tau_L$, where J is the strength of

antiferromagnetic interaction and τ_L is the characteristic lifetime, can serve as a measure to quantify how well the coherent oscillations are preserved. In our scheme, the characteristic lifetime τ_L is the lifetime of the Rydberg-dressed states τ_{dress} , which is approximately 60 ms according to Sec. S-3. And the strength of NN spin-spin interaction, J_{ex} and J_z , is about 2 kHz from the calculation in Sec. S-5, which gives

$$J\tau_L = J_{\text{ex}}(J_z)\tau_{\text{dress}} \approx 2\pi \times 120\hbar. \quad (\text{S19})$$

In contrast, the characteristic lifetime τ_L in optical lattices is the lifetime of optical lattice denoted as τ_{OL} , reported to be on the order of 1 s [14]. To realize the two-dimensional t - J model which excludes double occupancy, the ratio of on-site repulsion strength U to the NN hopping amplitude t must be tuned to drive the Fermi-Hubbard model into Mott regime, generating the effective spin-spin interaction $J = 4t^2/U$. For typical optical lattices in the harmonic trap, the Mott transition occurs at $U/t \approx 20$ on the edge of system, while the entire system enters into Mott phase at $U/t \approx 80$ [105, 106]. The typical value for t can be estimated as 1 kHz, which gives

$$J\tau_L = \frac{4t^2}{U}\tau_{\text{OL}} \approx 2\pi \times 50\hbar \sim 2\pi \times 200\hbar. \quad (\text{S20})$$

The comparison demonstrates that our scheme performs comparably to the Fermi-Hubbard model in optical lattice in the harmonic trap, sufficient for the simulation of t - J model.

B. Total operation time v.s. lifetime of tweezers

Secondly, we analyze the restriction from the lifetime of tweezers (denoted as τ_{tweezer}). The total operation time can be divided into two parts: time for gate operations (denoted as τ_{gate}) and time for tweezer movements (denoted as τ_{move}). We estimate the time for gate operation, τ_{gate} , as

$$\tau_{\text{gate}} \approx \left(1 + \frac{2\tau_{t,\text{N}} + 2\tau_{t',\text{NN}}}{\tau_J}\right)\tau_{\text{dress}}, \quad (\text{S21})$$

where $2\tau_{t,\text{N}}$, $2\tau_{t',\text{NN}}$ and τ_J are the operation times for $H_{t,\text{N}}$, $H_{t',\text{NN}}$ and H_J per cycle, and $\tau_{\text{dress}} \approx 60$ ms is the lifetime of the Rydberg-dressed states. We analysis the ratio $2\tau_{t,\text{N}}/\tau_J$, $2\tau_{t',\text{NN}}/\tau_J$ in two main applications of our scheme: probing the d-wave superconductivity and high T_c physics, where $t > J$, and simulating the non-trivial dynamics related to the Hilbert space fragmentation, where $t \ll J$. Based on the previous experiment [65], the inter-tweezer hopping amplitude can be tuned to exceed 0.3 kHz, while the strength of J in our realization is about 2 kHz, as shown in Sec. S-5. To realize typical model parameters for high- T_c superconductivity, it requires $2\tau_{t,\text{N}}/\tau_J \approx 10$ and $2\tau_{t',\text{NN}}/\tau_J \approx 1$, leading to a gate operation time $\tau_{\text{gate}} \approx 0.7$ s. On the other hand, for the $J/t \gg 1$ regime to realize Hilbert space fragmentation, only $2\tau_{t,\text{N}}/\tau_J \approx 1$ and $\tau_{t',\text{NN}} = 0$ are required, resulting in a significantly shorter gate operation time $\tau_{\text{gate}} \approx 0.12$ s.

Next, we estimate the time for tweezer movement, τ_{move} , as

$$\tau_{\text{move}} \approx N_{\text{move}}\tau_{1\text{move}}, \quad (\text{S22})$$

where N_{move} is the total number of tweezer movements, and $\tau_{1\text{move}}$ is the time required for a single movement. To ensure that the higher-order contributions in the Suzuki-Trotter decomposition are negligible, we divide the total simulation procedure into about 3000 cycles with $\tau_J \approx 20$ μ s, yielding $N_{\text{move}} \approx 10^4$. For the estimation of $\tau_{1\text{move}}$, we consider a typical lattice configuration, a 10×10 square lattice. The length scale for a single tweezer movement within this lattice is approximately 100 μ m with the selected lattice spacing $a = 8.2$ μ m in Sec. S-5, which gives $\tau_{1\text{move}} \approx 200$ μ s to maintain quantum coherence [62, 63]. Thus, we estimate $\tau_{\text{move}} \approx 2$ s for a 10×10 lattice.

Consequently, the total time required for our scheme, estimated as $\tau_{\text{gate}} + \tau_{\text{move}}$, is on the order of several seconds for moderate-sized lattices, which is significantly shorter than the lifetime of the tweezers, $\tau_{\text{tweezer}} \sim 10^3$ s at 4 K [92, 93].

S-7. HILBERT SPACE FRAGMENTATION AND PARAMETER CONDITIONS

In the main text, we demonstrate that when $J/t \gg 1$, Hilbert space fragmentation (HSF) arises. In this section, we derive more detailed criteria for t and J to ensure robust HSF by comparing the effective transition amplitude and

energy splitting. Specifically, we investigate the Krylov subspace of the one-dimensional t - J model in the $J/t \gg 1$ regime, composed of entangled spin bound states $|A\rangle$, $|B\rangle$ and $|C\rangle$. The kinetic part of the Hamiltonian is given by

$$H_t = \sum_{i,\sigma} (-t P_i c_{i,\sigma}^\dagger c_{i+1,\sigma} P_{i+1} + \text{H.c.}) \quad (\text{S23})$$

where $P_i = 1 - n_{i,\uparrow} n_{i,\downarrow}$ is the projection operator excluding double occupancy on site i , and $n_{i,\uparrow}$ and $n_{i,\downarrow}$ are the density operators of spin-up and spin-down states. This kinetic term can induce transitions from the initial states $|I\rangle$ within the Krylov subspace to final states $|F\rangle$ outside the Krylov subspace. These undesirable transitions may disrupt the fragmented Krylov subspace and therefore should be suppressed. Our analysis focuses on the potential first-order and second-order undesirable transitions, as the higher-order transitions are weaker effects and will be typically blocked by the effective energy splitting, as elucidated by the self-pinning effect in Sec. S-8.

A. First-order transition channels

$ I\rangle$	$ F\rangle$	$\Omega_{I \rightarrow F}^{(1)}$	$\delta E^{(0)}$
$ \dots 0B0 \dots\rangle$	$ \dots 0A0\downarrow 0 \dots\rangle$	$\frac{\sqrt{3}}{2}t$	$\frac{1}{2}J$
$ \dots 0A0A0 \dots\rangle$	$ \dots 0B0\uparrow 0 \dots\rangle$	$-\frac{\sqrt{6}}{4}t$	$\frac{1}{2}J$
$ \dots 0B0C0 \dots\rangle$	$ \dots 0D_10A0 \dots\rangle$	$-0.5915t$	$0.3660J$
$ \dots 0B0C0 \dots\rangle$	$ \dots 0D_10T0 \dots\rangle$	$0.1972t$	$0.6340J$
$ \dots 0B0C0 \dots\rangle$	$ \dots 0D_20A0 \dots\rangle$	$0.5576t$	$0.2929J$
$ \dots 0B0B0 \dots\rangle$	$ \dots 0D_10\downarrow\downarrow 0 \dots\rangle$	$-0.2788t$	$0.6340J$
$ \dots 0B0B0 \dots\rangle$	$ \dots 0D_30A0 \dots\rangle$	$-0.7886t$	$0.2929J$

TABLE S-XI. Relevant first-order transition channels between the initial states $|I\rangle$ and the final states $|F\rangle$ with the corresponding transition amplitude $\Omega_{I \rightarrow F}^{(1)}$ and the difference of bound energies $\delta E^{(0)}$. For channels related by spin inversion symmetry and spatial inversion symmetry, only one representative is listed. Here $|T\rangle = (|\uparrow\downarrow\rangle - |\downarrow\uparrow\rangle)/\sqrt{2}$ is the spin triplet state, D_1 and D_2 are two kinds of four-body spin bound states consisting of two $|\uparrow\rangle$ and two $|\downarrow\rangle$ states, and D_3 is a four-body spin bound state consisting of one $|\uparrow\rangle$ and three $|\downarrow\rangle$ states.

Firstly, we investigate the first-order transition channels between initial states $|I\rangle$ and $|F\rangle$ with the bound energies E_I and E_F , respectively. The first-order effective transition amplitude is given by

$$\Omega_{I \rightarrow F}^{(1)} = \langle F | H_t | I \rangle. \quad (\text{S24})$$

The effective energy splitting ΔE between $|I\rangle$ and $|F\rangle$ mainly results from the difference of bound energies $\delta E^{(0)}$:

$$\Delta E = \delta E^{(0)} = E_F - E_I. \quad (\text{S25})$$

The higher-order energy corrections of $|I\rangle$ and $|F\rangle$ induced by H_t are small compared to $\delta E^{(0)}$ for the relevant first-order transition channels, so $\delta E^{(0)}$ is the primary contributor to the effective energy splitting. The suppression of undesirable first-order transition channels requires

$$|\Omega_{I \rightarrow F}^{(1)}| \ll |\Delta E| = |\delta E^{(0)}|. \quad (\text{S26})$$

We list all the relevant first-order transition channels satisfying $|\delta E^{(0)}| < J$ with the corresponding effective transition amplitude $\Omega_{I \rightarrow F}^{(1)}$ and the difference between bound energies $\delta E^{(0)}$ in Table S-XI, which gives the criteria

$$\frac{t}{J} \ll 0.3714. \quad (\text{S27})$$

B. Second-order transition channels

Secondly, we investigate the second-order transition channels between initial states $|I\rangle$ and $|F\rangle$ with the bound energies E_I and E_F , respectively. Since the second-order transitions are weaker compared to the first-order ones,

$ I\rangle$	$ F\rangle$	$\Omega_{I \rightarrow F}^{(2)}$	$\delta E^{(0)}$	$\delta E_I^{(2)}$	$\delta E_F^{(2)}$
$ \dots 00B0C00 \dots\rangle$	$ \dots 00E0\downarrow 00 \dots\rangle$	$-0.252t^2/J$	$-0.0721J$	$-3.8938t^2/J$	$-1.7557t^2/J$
$ \dots 00C0B00 \dots\rangle$	$ \dots 00E0\downarrow 00 \dots\rangle$	$-0.252t^2/J$	$-0.0721J$	$-3.8938t^2/J$	$-1.7557t^2/J$
$ \dots 00C0C00 \dots\rangle$	$ \dots 00E0\uparrow 00 \dots\rangle$	$-0.183t^2/J$	$-0.0721J$	$-8.1399t^2/J$	$-3.2479t^2/J$

TABLE S-XII. Relevant second-order transition channels between the initial states $|I\rangle$ and the final states $|F\rangle$ with the corresponding transition amplitude $\Omega_{I \rightarrow F}^{(2)}$, difference of bound energies $\delta E^{(0)}$, and the second-order energy corrections $\delta E_I^{(2)}$ and $\delta E_F^{(2)}$. For channels related by spin inversion symmetry and spatial inversion symmetry, only one representative is listed. Here E is a five-body spin bound state consisting of three $|\uparrow\rangle$ and two $|\downarrow\rangle$ states.

only the nearly resonant second-order transition channels are considered here. The second-order effective transition amplitude is given by

$$\Omega_{I \rightarrow F}^{(2)} = \sum_{E_{IS_1} \neq E_I} \frac{\langle F | H_t | IS_1 \rangle \langle IS_1 | H_t | I \rangle}{E_I - E_{IS_1}}, \quad (S28)$$

where $|IS_1\rangle$ represents the intermediate states involved in the perturbation calculation of $\Omega_{I \rightarrow F}^{(2)}$ with bound energy E_{IS_1} . For the nearly resonant transitions, the energy correction induced by H_t can not be neglected in comparison to the difference of bound energies $\delta E^{(0)} = E_F - E_I$, and the second-order energy corrections for $|I\rangle$ and $|F\rangle$ are given by

$$\begin{aligned} \delta E_I^{(2)} &= \sum_{E_{IS_2} \neq E_I} \frac{\langle I | H_t | IS_2 \rangle \langle IS_2 | H_t | I \rangle}{E_I - E_{IS_2}}, \\ \delta E_F^{(2)} &= \sum_{E_{IS_3} \neq E_I} \frac{\langle F | H_t | IS_3 \rangle \langle IS_3 | H_t | F \rangle}{E_I - E_{IS_3}}, \end{aligned} \quad (S29)$$

where $|IS_2\rangle$ and $|IS_3\rangle$ are the intermediate states with energies E_{IS_2} and E_{IS_3} , relevant in the perturbative calculation of $\delta E_I^{(2)}$ and $\delta E_F^{(2)}$ respectively. We include the contribution of $\delta E_I^{(2)}$ and $\delta E_F^{(2)}$ in the effective energy splitting. The comparison between the effective transition amplitude and the effective energy splitting requires

$$|\Omega_{I \rightarrow F}^{(2)}| \ll |\Delta E| = |\delta E^{(0)} + \delta E_F^{(2)} - \delta E_I^{(2)}|. \quad (S30)$$

We list all the relevant second-order transition channels satisfying $|\delta E^{(0)}| < 0.1J$ with the corresponding effective transition amplitude $\Omega_{I \rightarrow F}^{(2)}$, difference of bound energies $\delta E^{(0)}$ and the second-order energy corrections $\delta E_I^{(2)}$ and $\delta E_F^{(2)}$ in Table S-XII, which gives the criteria

$$\frac{t^2}{J} \ll \min(|0.2861J - 8.4845\frac{t^2}{J}|, |0.394J - 26.7322\frac{t^2}{J}|). \quad (S31)$$

Assuming $0.2861J - 8.4845t^2/J, 0.394J - 26.7322t^2/J > 0$, the Ineq. (S31) can be further simplified as

$$\frac{t^2}{J^2} \ll 0.01474. \quad (S32)$$

For most cases, if Ineq. (S32) is satisfied, Ineq. (S27) is also satisfied. But for accuracy, we choose to keep both Ineq. (S27) and Ineq. (S32) as the criteria to ensure robust HSF and associated many-body self-pinning effect.

S-8. GENERAL THEORY OF THE MANY-BODY SELF-PINNING EFFECT

In this section, we present a general theory for the many-body self-pinning effect. A general interacting Hamiltonian with kinetic part H_{kin} and interaction part H_{int} is given by

$$H = \alpha_{\text{kin}} H_{\text{kin}} + \alpha_{\text{int}} H_{\text{int}}, \quad (S33)$$

where α_{kin} and α_{int} are the tuning parameters controlling the relative contributions of the kinetic and interaction terms. We analyze this Hamiltonian in the strong coupling regime $|\alpha_{\text{int}}/\alpha_{\text{kin}} \gg 1|$. In this regime, the interaction

term dominates the Hamiltonian, and α_{int} emerges as the dominant energy scale. The bound states $|Q\rangle$, defined as the eigenstate of $\alpha_{\text{int}}H_{\text{int}}$ without empty sites, thus serve as the fundamental units in quantum dynamics. The general form of the eigenstates $|\phi_I\rangle$ of $\alpha_{\text{int}}H_{\text{int}}$ can be represented as a series of bound states Q_i separated by empty states, which is given by

$$|\phi_I\rangle = |\cdots 0Q_1 0 \cdots 0Q_2 0 \cdots \cdots 0Q_i 0 \cdots \rangle. \quad (\text{S34})$$

The term $\alpha_{\text{kin}}H_{\text{kin}}$ generates transitions that preserve the energies of the eigenstates. The dynamics involving $|\phi_I\rangle$ induced by $\alpha_{\text{kin}}H_{\text{kin}}$ can be described by the effective Hamiltonian

$$H_{\phi}^{\text{eff}} = \sum_{n=1,2,3,\dots} \alpha_{\text{kin}} H_{\text{kin}} (G_{\text{int}} \alpha_{\text{kin}} H_{\text{kin}})^{n-1} = \sum_{n=1,2,3,\dots} (\alpha_{\text{kin}})^n H_{\text{kin}} (G_{\text{int}} H_{\text{kin}})^{n-1}, \quad (\text{S35})$$

where $G_{\text{int}} = (1 - P_{\phi})(E_{\phi} - \alpha_{\text{int}}H_{\text{int}})^{-1}(1 - P_{\phi})$. Here, P_{ϕ} is the projection operator in the subspace spanned by $|\phi_I\rangle$, and E_{ϕ} is the unperturbed energy. Since $G_{\text{int}} \propto \alpha_{\text{int}}^{-1}$, the n th-order term of H_{ϕ}^{eff} scales as

$$H_{\phi}^{\text{eff}} \propto \frac{\alpha_{\text{kin}}^n}{\alpha_{\text{int}}^{n-1}}. \quad (\text{S36})$$

For two resonant eigenstates $|\phi_{I1}\rangle$ and $|\phi_{I2}\rangle$, the effective transition amplitude λ_{eff} and effective energy splitting δ_{eff} are derived from the off-diagonal and diagonal matrix elements of H_{ϕ}^{eff} as

$$\begin{aligned} \lambda_{\text{eff}} &= \langle \phi_{I1} | H_{\phi}^{\text{eff}} | \phi_{I2} \rangle = \sum_{n=n_0^{\lambda}, n_0^{\lambda}+1, \dots} g_n^{\lambda} \frac{\alpha_{\text{kin}}^n}{\alpha_{\text{int}}^{n-1}}, \\ \delta_{\text{eff}} &= \langle \phi_{I1} | H_{\phi}^{\text{eff}} | \phi_{I1} \rangle - \langle \phi_{I2} | H_{\phi}^{\text{eff}} | \phi_{I2} \rangle = \sum_{n=n_0^{\delta}, n_0^{\delta}+1, \dots} g_n^{\delta} \frac{\alpha_{\text{kin}}^n}{\alpha_{\text{int}}^{n-1}}, \end{aligned} \quad (\text{S37})$$

where n_0^{λ} and n_0^{δ} are the leading perturbative orders of λ_{eff} and δ_{eff} , respectively. The quantum dynamics is determined by the comparison between δ_{eff} and λ_{eff} :

$$\frac{\delta_{\text{eff}}}{\lambda_{\text{eff}}} = f(g_n^{\lambda}, g_n^{\delta}) \times \frac{g_{n_0^{\delta}}^{\delta} (\alpha_{\text{kin}})^{n_0^{\delta} - n_0^{\lambda}}}{g_{n_0^{\lambda}}^{\lambda} (\alpha_{\text{int}})^{n_0^{\delta} - n_0^{\lambda}}}, \quad f(g_n^{\lambda}, g_n^{\delta}) = \frac{1 + \sum_{i=1,2,\dots} (g_{n_0^{\delta}+i}^{\delta} / g_{n_0^{\delta}}^{\delta}) (\alpha_{\text{kin}} / \alpha_{\text{int}})^i}{1 + \sum_{i=1,2,\dots} (g_{n_0^{\lambda}+i}^{\lambda} / g_{n_0^{\lambda}}^{\lambda}) (\alpha_{\text{kin}} / \alpha_{\text{int}})^i}. \quad (\text{S38})$$

Here $f(g_n^{\lambda}, g_n^{\delta})$ summarizes the contribution of higher-order perturbations. In the strong coupling regime $|\alpha_{\text{int}} / \alpha_{\text{kin}}| \gg 1$, we have $f(g_n^{\lambda}, g_n^{\delta}) \approx 1$, and the ratio $\delta_{\text{eff}} / \lambda_{\text{eff}}$ in Eq. (S38) simplifies to

$$\lim_{|\alpha_{\text{I}} / \alpha_{\text{K}}| \rightarrow \infty} \frac{\delta_{\text{eff}}}{\lambda_{\text{eff}}} = \begin{cases} \infty, & n_0^{\lambda} > n_0^{\delta}, \\ g_{n_0^{\delta}}^{\delta} / g_{n_0^{\lambda}}^{\lambda}, & n_0^{\lambda} = n_0^{\delta}, \\ 0, & n_0^{\lambda} < n_0^{\delta}. \end{cases} \quad (\text{S39})$$

When $n_0^{\lambda} > n_0^{\delta}$, the effective transition amplitude λ_{eff} is negligible compared to the effective energy splitting δ_{eff} , and the transition between $|\phi_{I1}\rangle$ and $|\phi_{I2}\rangle$ is completely blocked. When $n_0^{\lambda} = n_0^{\delta}$, the effective transition amplitude λ_{eff} is comparable to the effective energy splitting δ_{eff} , and the transition between $|\phi_{I1}\rangle$ and $|\phi_{I2}\rangle$ can occur but is partially blocked. Only when $n_0^{\lambda} < n_0^{\delta}$ does the transition between $|\phi_{I1}\rangle$ and $|\phi_{I2}\rangle$ occur freely. Thus, when $n_0^{\lambda} \geq n_0^{\delta}$, quantum states will be completely or partially pinned to its initial configurations, despite the presence of other resonant states. We term this novel phenomenon the many-body self-pinning effect.

This fact partly explains why, in Sec. S-7, only first-order and second-order undesirable transition channels are considered. The effective energy splitting is generally a second-order process with $n_0^{\delta} = 2$. Therefore, higher-order transitions with $n_0^{\lambda} > 2$ will be completely blocked since $n_0^{\lambda} > n_0^{\delta}$. Consequently, these channels do not participate in the quantum dynamics relevant to spin bound states $|A\rangle$, $|B\rangle$ and $|C\rangle$ in the $J/t \gg 1$ regime.

S-9. MANY-BODY ELF-PINNING EFFECT IN THE t - J AND t - J_z MODEL

In this section, we apply the general theory outlined in Sec. S-8 to a typical Krylov subspace of the one-dimensional t - J model and t - J_z model in the strong coupling regime. The different behaviours exhibited in these two models indicate that local entanglement enforces the occurrence of the many-body self-pinning effect.

A. Self-Pinning in the t - J Model

Firstly, we investigate the self-pinning effect in the Krylov subspaces formed by entangled spin bound states $|A\rangle$, $|B\rangle$ and $|C\rangle$. The transitions permitted by the emergent conserved quantities occur between $3n$ $|A\rangle$ states and n $|B\rangle$, n $|C\rangle$ states. The effective energy splitting, typically a second-order process with $n_0^\delta = 2$, limits the unblocked transition channels to those with $n_0^\lambda \leq 2$.

A typical transition with $n_0^\lambda = 2$ between $|\cdots 00A0A0A00\cdots\rangle$ and $|\cdots 00B00C00\cdots\rangle$ is analyzed according to Eq. (S37) and (S39). Further calculations yield

$$g_2^\lambda = -3\sqrt{2}/2, \quad g_2^\delta = 4/3, \quad \delta_{\text{eff}}/\lambda_{\text{eff}} \approx 0.63. \quad (\text{S40})$$

This indicates that the effective energy splitting δ_{eff} and the effective transition amplitude λ_{eff} are comparable. Therefore, many-body self-pinning effects are anticipated in this Krylov subspace of the t - J model, partially obstructing transitions between resonant states $|\cdots 00A0A00\cdots\rangle$ and $|\cdots 00B00C00\cdots\rangle$.

B. Absence of Self-Pinning in the t - J_z Model

Before delving into the investigation of the many-body self-pinning effect within t - J_z model, we first analyze the Hamiltonian and its associated Hilbert space fragmentation (HSF). The t - J_z Hamiltonian is given by

$$H_{t-J_z} = \sum_{i,\sigma} (-t P_i c_{i,\sigma}^\dagger c_{i+1,\sigma} P_{i+1} + \text{H.c.}) + \sum_i J_z S_{z,i} S_{z,i+1}, \quad (\text{S41})$$

where $P_i = 1 - n_{i,\uparrow} n_{i,\downarrow}$ is the projection operator excluding double occupancy on site i , and $n_{i,\uparrow}$ and $n_{i,\downarrow}$ are the density operators of spin-up and spin-down states, respectively. Due to the kinetic constraint of the t - J_z model, the spin pattern of a product state becomes a conserved quantity [98]. We consider the Krylov subspace characterized by the spin pattern “ $\uparrow\downarrow\uparrow\downarrow\cdots$ ”, comprising an equal number of $|\uparrow\rangle$ and $|\downarrow\rangle$ states. In the $J_z/t \gg 1$ regime, the bound states of t - J_z model are product states, and the Krylov subspace with spin pattern “ $\uparrow\downarrow\uparrow\downarrow\cdots$ ” further splits into smaller Krylov subspaces with the emergent conserved quantity N_{BS} , representing the number of product spin bound states. For instance, if there are five lattice sites and the conserved spin pattern is “ $\uparrow\downarrow\uparrow\downarrow$ ”, the three bases of the Krylov subspace labeled by emerged conserved quantity $N_{\text{BS}} = 2$ are $|\uparrow 0\downarrow\downarrow\rangle$, $|\downarrow\downarrow 0\uparrow\downarrow\rangle$ and $|\uparrow\downarrow\uparrow 0\downarrow\rangle$.

Subsequently, we demonstrate the absence of self-pinning in the typical Krylov subspace characterized by spin pattern “ $\uparrow\downarrow\uparrow\downarrow\cdots$ ” and emergent conserved quantity N_{BS} . The leading perturbative orders satisfy $n_0^\lambda < n_0^\delta$, with

$$n_0^\lambda = 1, \quad n_0^\delta \geq 2. \quad (\text{S42})$$

Here, the typical transitions occur via the alteration of a single spin at the boundary of the product spin bound states, exemplified by the resonant transition between

$$|\cdots \uparrow\downarrow 0\uparrow\downarrow\cdots\rangle \longleftrightarrow |\cdots \uparrow\downarrow\uparrow 0\downarrow\cdots\rangle. \quad (\text{S43})$$

Consequently, the typical transition corresponds to $n_0^\lambda = 1$. But the leading perturbative order of the effective energy splitting n_0^δ remains equal to two, e.g., the transition between

$$|\cdots 00\uparrow\downarrow 0\uparrow\downarrow 00\cdots\rangle \longleftrightarrow |\cdots 00\uparrow 0\downarrow\uparrow\downarrow 00\cdots\rangle, \quad (\text{S44})$$

or even larger than two, e.g., the transition between

$$|\cdots 00\uparrow\downarrow\uparrow 0\downarrow\uparrow\downarrow 00\cdots\rangle \longleftrightarrow |\cdots 00\uparrow\downarrow 0\uparrow\downarrow\uparrow\downarrow 00\cdots\rangle, \quad (\text{S45})$$

resulting $n_0^\lambda < n_0^\delta$. Therefore, the many-body self-pinning effect is predicted to vanish in this Krylov subspace of the t - J_z model, allowing free transitions between different product spin bound states.

C. Comparison Between t - J and t - J_z Models

Upon comparing the t - J and t - J_z models, we observe that local entanglement of the bound states in the t - J model effectively suppresses low-order transition channels, resulting in a higher n_0^λ and facilitating the self-pinning. This is because entangled states involve multi-particle correlations, typically requiring transitions beyond single-particle transfers to change configurations. For instance, the energy mismatch in the t - J model between entangled bound states typically inhibits first-order resonant transitions with $n_0^\lambda = 1$. In contrast, for product bound states in the t - J_z model, resonant transitions remain feasible as long as the local bond structure remains unchanged between the initial and final configurations. This demonstrates the local entanglement enforces the many-body self-pinning effect.

S-10. SUPPLEMENTARY SIMULATIONS ON THERMALIZATION RELATED DYNAMICS

In this section, we provide additional numerical simulations for the t - J and t - J_z model in the $J/t, J_z/t \gg 1$ regime on the quantum dynamics related to the Krylov-restricted thermalization, as a supplementary for the numerical simulation presented in the main text. All simulations in this section are based on the time-evolving block decimation (TEBD) method in the Tenpy library [103].

Firstly, we compare the long-time averages of the multi-site density correlations and sublattice entanglement entropy (EE) in t - J model. The different resonant initial states is composed of the same spin bound states, while arranged in different orders. As shown Fig. S4, the long-time averages converge to similar values for these initial states, indicating the outcome of long-time evolution of these states may be described by a single statistical ensemble. This is reasonable since for states composed of the same bound states, the effective energy corrections are the same, leading to the vanishing of effective energy splitting.

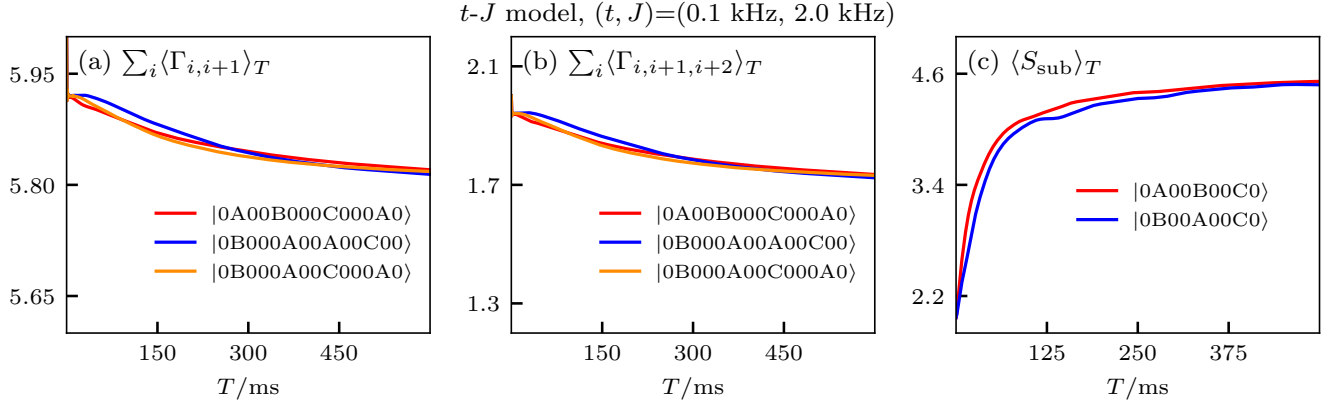


FIG. S4. Comparison for t - J model across initial states composed of the same spin bound states but arranged in different orders. Long-time averages of the density correlations ($\Gamma_{i,i+1} = n_i n_{i+1}$, $\Gamma_{i,i+1,i+2} = n_i n_{i+1} n_{i+2}$) and sublattice entanglement entropy (EE) are calculated with parameters $t=0.1$ kHz and $J=2.0$ kHz. (a-b) shows the long-time averages of density correlations for a 20-site t - J chain. (c) shows the long-time averages of sublattice EE for a 14-site t - J chain. The long-time average values converge to similar values. The bond dimension for TEBD simulation keeps up to 800 for (a-b), 400 for (c).

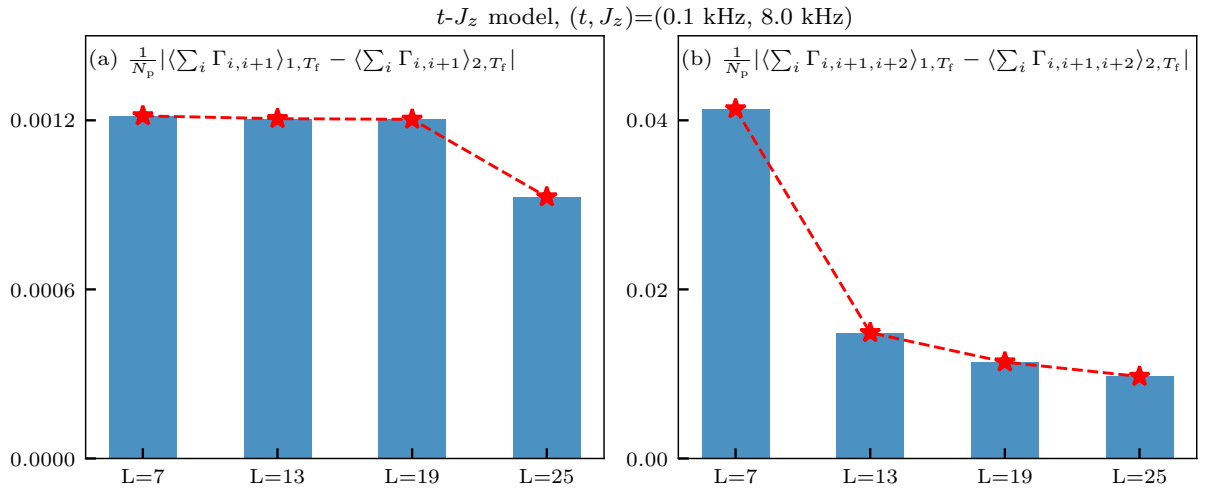


FIG. S5. Normalized discrepancies of the long-time averages of the density correlations in the t - J_z model with different number of sites. Two kinds of initial states are $|\mathbf{a}\mathbf{a}\cdots\mathbf{a}0\rangle$ and $|\mathbf{b}\mathbf{b}\cdots\mathbf{b}0\rangle$, where \mathbf{a} and \mathbf{b} represent the spin pattern “ $0\uparrow\downarrow 0\uparrow\downarrow$ ” and “ $0\uparrow 0\downarrow\uparrow\downarrow$ ”. And the site number L is chosen as 7, 13, 19, 25 with parameters $t = 0.1$ kHz and $J = 8.0$ kHz. The total time of evolution T_F is 600 ms. (a) The normalized discrepancies of long-time averages of $\Gamma_{i,i+1} = n_i n_{i+1}$ (b) The normalized discrepancies of long-time average of $\Gamma_{i,i+1,i+2} = n_i n_{i+1} n_{i+2}$. The bond dimension for TEBD simulation keeps up to 8,50,306,500 for $L = 7, 13, 19, 25$.

Secondly, we compare the normalized discrepancies of the long-time averages of the density correlations in t - J_z model with different number of sites and find some signatures of Krylov-restricted thermalization. The normalized discrepancy of operator O is defined as

$$\frac{1}{N_p} |\langle O \rangle_{1,T_f} - \langle O \rangle_{2,T_f}| = \frac{1}{N_p} \left| \frac{1}{T_F} \int_0^{T_F} dt (\langle \psi_1(t) | O | \psi_1(t) \rangle - \langle \psi_2(t) | O | \psi_2(t) \rangle) \right|, \quad (\text{S46})$$

where $|\psi_1(0)\rangle$ and $|\psi_2(0)\rangle$ are two resonant initial states with particle number N_p , and T_F is the total time of evolution. For t - J_z model, we choose two kinds of resonant initial states denoted as $|\mathbf{aa} \cdots \mathbf{a}0\rangle$ and $|\mathbf{bb} \cdots \mathbf{b}0\rangle$, where \mathbf{a} and \mathbf{b} represent the spin pattern “ $0\uparrow\downarrow 0\uparrow\downarrow$ ” and “ $0\uparrow 0\downarrow\uparrow\downarrow$ ”. As shown in Fig. S5, the normalized discrepancies diminish as the number of sites increase. This result confirms that non-thermalization is mitigated in the t - J_z model compared to the t - J model, and suggests that Krylov-restricted thermalization may occur for t - J_z model.

S-11. SUPPLEMENTARY SIMULATIONS ON ENTANGLEMENT RELATED DYNAMICS

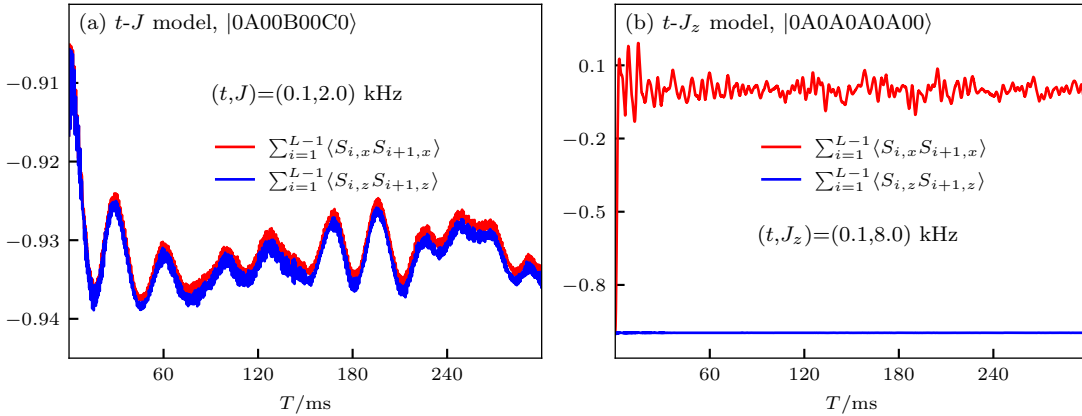


FIG. S6. Comparison between t - J and t - J_z model: S_x and S_z correlations. For t - J model, S_x and S_z correlations remain isotropic. In contrast, the S_x correlations decay to zero while the S_z correlations remain finite in the t - J_z model. (a) corresponds to a 14-site t - J chain with parameters $t = 0.1$ kHz and $J = 2.0$ kHz. The initial state is $|0A00B00C0\rangle$. (b) corresponds to a 14-site t - J_z chain with parameters $t = 0.1$ kHz and $J_z = 8.0$ kHz. The initial state is $|0A0A0A0A00\rangle$. For both (a) and (b), The bond dimension for TEBD simulation keeps up to 500.

In this section, we provide additional numerical simulations for the t - J and t - J_z model in the $J/t, J_z/t \gg 1$ regime on some non-trivial quantum dynamics, highlighting the significance of the local spin entanglement. All simulations in this section are also based on the time-evolving block decimation (TEBD) method in the Tenpy library [103].

Firstly, we compare the expectation values of S_x and S_z correlations (defined as $\langle S_{i,x} S_{i+1,x} \rangle$ and $\langle S_{i,z} S_{i+1,z} \rangle$) in the time evolution of t - J and t - J_z model, demonstrating the key influence of local spin entanglement. Special initial states are selected to satisfy $\sum_i \langle S_{i,x} S_{i+1,x} \rangle = \sum_i \langle S_{i,z} S_{i+1,z} \rangle$ for both models. As depicted in Fig. S6(a), the S_x and S_z correlations remain isotropic in the t - J model:

$$\sum_i \langle S_{i,x} S_{i+1,x} \rangle = \sum_i \langle S_{i,z} S_{i+1,z} \rangle. \quad (\text{S47})$$

In contrast, for the t - J_z model in Fig. S6(b), the S_x correlations decay to zero while the S_z correlations remain finite:

$$\sum_i \langle S_{i,x} S_{i+1,x} \rangle \rightarrow 0, \quad \sum_i \langle S_{i,z} S_{i+1,z} \rangle \rightarrow \text{Const.} \quad (\text{S48})$$

The discrepancy between t - J and t - J_z model can be attributed to the local spin entanglement. For t - J model, all entangled spin bound states $|\mathbf{A}\rangle$, $|\mathbf{B}\rangle$ and $|\mathbf{C}\rangle$ satisfy $\langle \sum_i S_{i,x} S_{i+1,x} \rangle = \langle \sum_i S_{i+1,z} S_{i,z} \rangle$, thereby preserving information of short-range spin entanglement through these bound states. Conversely, for the t - J_z model, while the singlet state $|\mathbf{A}\rangle$ is an eigenstate of the interaction part of the Hamiltonian, the product state $|\uparrow\downarrow\rangle$ and $|\downarrow\uparrow\rangle$ are also degenerate eigenstates. When two singlet states $|\mathbf{A}\rangle$ approach each other, the spin-spin interaction introduces two components

$|\uparrow\downarrow\rangle$ and $|\downarrow\uparrow\rangle$ with different phase factors. The accumulated chaotic phase factors leads to the decoherence of the system and the breakdown of the singlet state $|A\rangle$. Consequently, the system can be described by a statistical mixture of product states $|\uparrow\downarrow\rangle$ and $|\downarrow\uparrow\rangle$, resulting in the loss of information on short-range spin entanglement and a reduction in S_x correlation. In contrast, for the t - J model, destruction of the singlet state $|A\rangle$ into $|\uparrow\downarrow\rangle$ and $|\downarrow\uparrow\rangle$ suffers an energy cost due to local spin entanglement, thus suppressing the decoherence process.

This mechanism also significantly influences the density distribution during the time evolution of t - J and t - J_z model. As illustrated in Fig. S7(a), the time evolution of the density distribution with the t - J model exhibits a more coherent feature than that with the t - J_z model in Fig. S7(b). This observation further confirms that the outcome of long-time evolution of the initial spin bound states in the t - J_z model resembles a statistical mixture of different product states, while the long-time evolution in the t - J model retains more information due to local spin entanglement.

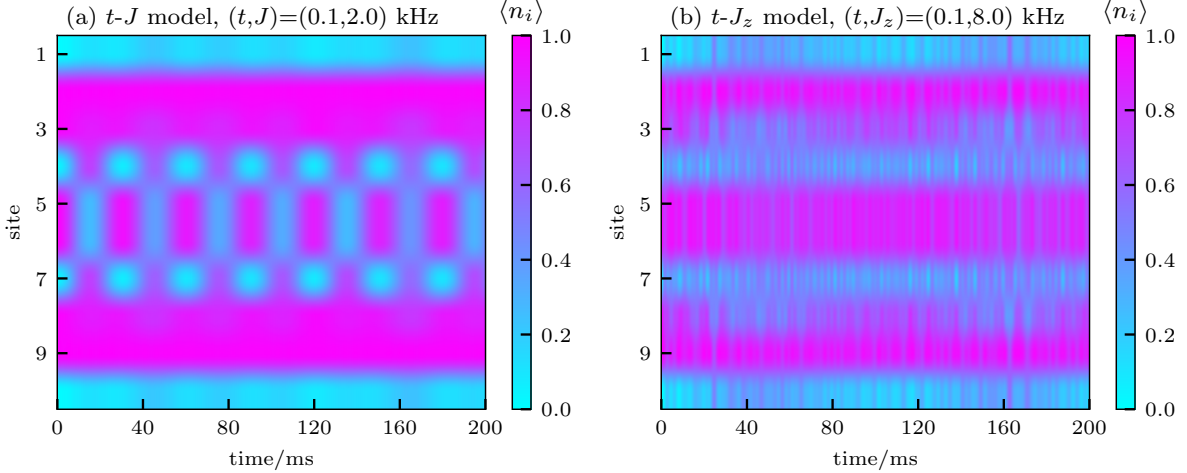


FIG. S7. Comparison between t - J model and t - J_z model: density distributions. The density distribution behaves more coherently than that of t - J_z model. (a) corresponds to a 10-site t - J chain with parameters $t = 0.1$ kHz and $J = 2.0$ kHz. (b) corresponds to a 10-site t - J_z chain with parameters $t = 0.1$ kHz and $J_z = 8.0$ kHz. For both (a) and (b), the initial state is $|0A0A0A0\rangle$. And the bond dimension for TEBD simulation keeps up to 300 for (a), 96 for (b).

S-12. NUMERICAL SIMULATION OF THE EXPERIMENTALLY RELEVANT MODEL

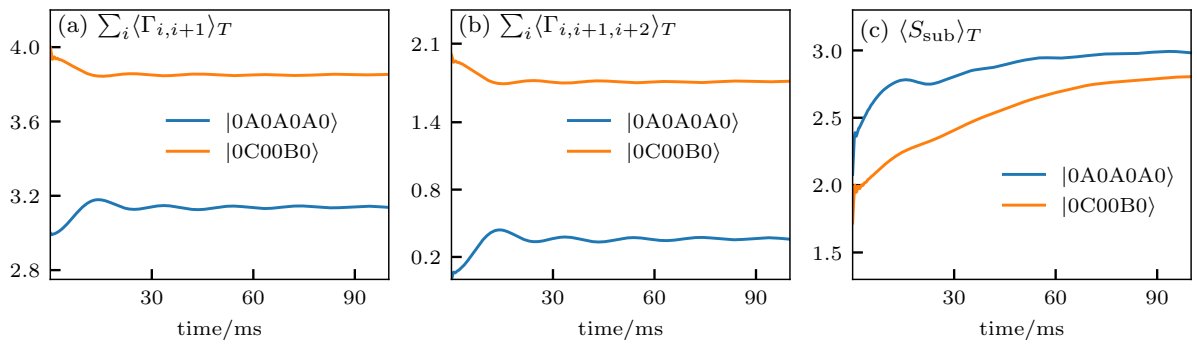


FIG. S8. Breakdown of Krylov-restricted thermalization in the experimentally relevant 10-site extended t - J chain with parameters $t = 0.1$ kHz. Other parameters are shown in Table S-IX and Table S-X. Similar phenomena discussed in the main text is also observed here. (a) and (b) correspond to the long-time averages of the density correlations for different quasi-resonant initial states. For (a), $\Gamma_{i,i+1} = n_i n_{i+1}$, and for (b), $\Gamma_{i,i+1,i+2} = n_i n_{i+1} n_{i+2}$. (c) corresponds to the long-time averages of the sublattice EE for different quasi-resonant initial states.

In the main text, we demonstrate the HSF and nonthermal dynamics in ideal t - J model. In this section, we demonstrate that the HSF and the nonthermal dynamics also exists in the experimentally relevant extended t - J chain. The main differences between the experimentally relevant model and the ideal t - J model is the density interaction $V_{\uparrow\uparrow}$, $V_{\downarrow\downarrow}$ induced by Rydberg vdW interaction, long-range interaction beyond the nearest-neighbour site, and a small anisotropy between J_{ex} and J_z . In Sec. S-5, we list the strength of spin-spin interaction J_{ex} , J_z and density-density interaction $V_{\uparrow\uparrow}$, $V_{\downarrow\downarrow}$ between different sites, with the experimentally reasonable lattice spacing $a = 8.2 \mu\text{m}$. For the lattice geometry of one-dimensional chain, it is reasonable to keep J_{ex} and J_z up to the next-nearest-neighbour interaction, and keep $V_{\uparrow\uparrow}$ and $V_{\downarrow\downarrow}$ up to the nearest-neighbour interaction, since longer-range terms are negligible.

Then we investigate the spin bound states $|A\rangle$, $|B\rangle$ and $|C\rangle$ in the experimentally relevant model, as the eigenstates of all the relevant interactions $J_{\text{ex},N}$, $J_{\text{ex},\text{NN}}$, $J_{z,N}$, $J_{z,\text{NN}}$, $V_{\uparrow\uparrow,N}$, $V_{\downarrow\downarrow,N}$. Here the subscripts N represent the nearest-neighbour interaction with the two-atom distance $x = 8.2 \mu\text{m}$, and the subscripts NN represent the next-nearest-neighbour interaction with the two-atom distance $x = 16.4 \mu\text{m}$. And the specific values of these interactions can be found in Table S-IX and Table S-X. In the experimentally relevant model, the corresponding wave functions and bound energies of spin bound states $|A\rangle$, $|B\rangle$ and $|C\rangle$ are

$$\begin{aligned} |A\rangle &= (|\uparrow\downarrow\rangle - |\downarrow\uparrow\rangle)/\sqrt{2}, & E_A &= -2.05865 \text{ kHz}, \\ |B\rangle &= 0.4107|\uparrow\downarrow\downarrow\rangle - 0.8140|\downarrow\uparrow\downarrow\rangle + 0.4107|\downarrow\downarrow\uparrow\rangle, & E_B &= -3.10548 \text{ kHz}, \\ |C\rangle &= 0.3951|\downarrow\downarrow\uparrow\rangle - 0.8293|\uparrow\downarrow\uparrow\rangle + 0.3951|\uparrow\uparrow\downarrow\rangle, & E_C &= -3.04809 \text{ kHz}. \end{aligned} \quad (\text{S49})$$

The spin bound state $|A\rangle$ remains the spin singlet state with minor corrections to its energy. In contrast, both the energies and wave functions of the spin bound state $|B\rangle$ and $|C\rangle$ will be slightly modified. The degeneracy relation $3E_A = E_B + E_C$ is not precisely established with a small discrepancy as $|3E_A - E_B - E_C| = 0.0224 \text{ kHz} \approx 0.01097 J_{\text{ex},N}$. If the amplitude of nearest-neighbour hopping t is not too small compared to the 0.0224 kHz discrepancy, three $|A\rangle$ and one $|B\rangle$, one $|C\rangle$ states can still be treated as quasi-degenerate states. Consequently, the nonthermal dynamics demonstrated in the main text can still be observed in the experimentally relevant model.

In Fig. S8, we repeat the numerical simulation of long-time average of density correlations and sublattice EE in the experimentally relevant extended t - J chain by exact diagonalization (ED) method in the QuSpin library [107, 108]. In real experiment, the lifetime of the dressed-Rydberg states is about 60 ms as listed in Sec. S-3. Therefore, we select a ten-site chain to ensure that our system can evolve into a regime near a steady state before the lifetime of the dressed-Rydberg state is exhausted. Despite the limited system size, we observe non-trivial nonthermal dynamics similar to those discussed in the main text, which may be detectable in future experiments.